Model constraints on the anthropogenic carbon budget of the Arctic Ocean

Jens Terhaar[1], James C. Orr[1], Marion Gehlen[1], Christian Ethé[2], and Laurent Bopp[3]

[1]Laboratoire des Sciences du Climat et de l'Environnement, LSCE/IPSL, CEA-CNRS-UVSQ, Université Paris-Saclay, 91191 Gif-sur-Yvette, France
[2]Institut Pierre et Simon Laplace, 4 Place Jussieu, 75005 Paris, France
[3]LMD/IPSL, Ecole Normale Supérieure / PSL Research University, CNRS, Ecole Polytechnique, Sorbonne Université, Paris, France

Correspondence to: Jens Terhaar (jens.terhaar@lsce.ipsl.fr)

Abstract. The Arctic Ocean is projected to experience not only amplified climate change but also amplified ocean acidification. Modeling future acidification depends on our ability to simulate baseline conditions and changes over the industrial era. Such centennial-scale changes require a global model to account for exchange between the Arctic and surrounding regions. Yet the coarse resolution of typical global models may poorly resolve that exchange as well as critical features of Arctic Ocean circulation. Here we assess how simulations of Arctic Ocean storage of anthropogenic carbon (C_{ant}), the main driver of open-ocean acidification, differ when moving from coarse to eddy admitting resolution in a global ocean circulation-biogeochemistry model (NEMO-PISCES). The Arctic's regional storage of C_{ant} is enhanced as model resolution increases. While the coarse-resolution model configuration ORCA2 (2°) stores 2.0 Pg C in the Arctic Ocean between 1765 and 2005, the eddy-admitting versions ORCA05 and ORCA025 (1/2° and 1/4°) store 2.4 and 2.6 Pg C. That result from ORCA025 falls within the uncertainty range from a previous data-based C_{ant} storage estimate (2.5 to 3.3 Pg C). Yet those limits may each need to be reduced by about 10% because data-based C_{ant} concentrations in deep waters remain at $\sim$6 μmol kg^{-1}, while they should be almost negligible by analogy to the near-zero observed CFC-12 concentrations from which they are calculated. Across the three resolutions, there was roughly three times as much anthropogenic carbon that entered the Arctic Ocean through lateral transport than via the flux of CO_2 across the air-sea interface. Wider comparison to nine earth system models that participated in the Coupled Model Intercomparison Project Phase 5 (CMIP5) reveals much larger diversity of stored anthropogenic carbon and lateral transport. Only the CMIP5 models with higher lateral transport obtain C_{ant} inventories that are close to the data-based estimates. Increasing resolution also enhances acidification, e.g., with greater shoaling of the Arctic's average depth of the aragonite saturation horizon during 1960–2012, from 50 m in ORCA2 to 210 m in ORCA025. To assess the potential to further refine modeled estimates of the Arctic Ocean's C_{ant} storage and acidification, sensitivity tests that adjust model parameters are needed given that century-scale global ocean biogeochemical simulations still cannot be run routinely at high resolution.

1 Introduction

The Arctic is experiencing amplified ocean acidification (Steinacher et al., 2009) and amplified climate change (Bekryaev et al., 2010), both of which may have consequences on the marine ecosystem (Gattuso and Hansson, 2011). The main driver of the ongoing acidification of the open ocean is the increase in atmospheric CO_2 during the industrial era and the ensuing uptake of

5 anthropogenic carbon from the atmosphere. Although this absorbed anthropogenic carbon cannot be measured directly, being dominated by the natural component, it has been estimated from other oceanographic data. For instance, Gruber et al. (1996) developed the $\Delta C^\star$ method, building on seminal studies (Brewer, 1978; Chen and Millero, 1979) and their criticism (Broecker et al., 1985) as well as large new global data sets with improved CO_2 system measurements. That back-calculation method first calculates the total dissolved inorganic carbon (C_T) at equilibrium with atmosphere before the water parcel is subducted.

10 That preformed C_T is then corrected for changes due to biological activity, as estimated from measurements of dissolved oxygen, total alkalinity (A_T), and nutrients, after which an estimate of preindustrial carbon is removed, finally yielding $\Delta C^\star$. In the high latitudes though, the $\Delta C^\star$ method's assumption of a constant air-sea CO_2 disequilibrium appears problematic (Orr et al., 2001). A second approach approximates the invasion of anthropogenic CO_2 into the interior ocean by a Transient Time Distribution (TTD) method, itself constrained by observations of transient-tracers such as CFC-12 or SF_6 (Hall et al., 2002;

15 Waugh et al., 2004). A third approach uses a Green's function instead of a TTD while also exploiting multiple transient tracers to assess the ocean's temporally changing distribution of anthropogenic carbon (Khatiwala et al., 2009). A comparison of these methods suggests that by 2010 the ocean had absorbed 155 ± 31 Pg C of anthropogenic carbon, around one-third of all emitted anthropogenic carbon (Khatiwala et al., 2013)

Less attention has been paid to anthropogenic carbon storage in the Arctic. Sabine et al. (2004) estimated that the Arctic

20 Ocean had absorbed 4.9 Pg C by 1994. Yet without estimates for anthropogenic carbon in the Arctic itself, Sabine et al. scaled the Arctic inventory to be 5% of their $\Delta C^\star$-based estimate for global anthropogenic carbon storage, assuming the same Arctic:Global ocean ratio as in the global gridded distribution of observed CFC-12 (Willey et al., 2004). More recently, Tanhua et al. (2009) used Arctic observations of CFC-11, CFC-12, and SF_6 and the TTD approach, revising the former Arctic anthropogenic carbon storage estimate downward to a range of 2.5 to 3.3 Pg C for year 2005. With that estimate, they emphasized

25 that while the Arctic Ocean represents only 1% of the global ocean volume, it stores 2% of the global ocean's anthropogenic carbon. Although these numbers are relatively small, Arctic concentrations of anthropogenic C_T must be relatively large, thus driving enhanced acidification in the Arctic Ocean.

To provide an alternate approach to estimate anthropogenic carbon in the Arctic and to assess its budget and the mechanisms that control it, we made carbon cycle simulations over the industrial era using a coupled ocean circulation-biogeochemical

30 model. A global-scale configuration is used to account for the Arctic in the context of the global carbon cycle, while avoiding artifacts from lateral boundary conditions that are needed for regional models. Simulations with the same model (NEMO-PISCES) are made at three resolutions, from coarse to eddy admitting, to help assess the extent to which coarse-resolution models may need to be improved to adequately simulate anthropogenic carbon storage in the Arctic Ocean.

Coarse resolution may be insufficient to adequately represent Arctic Ocean bathymetry, shelf, slopes, and ridges, all of which affect Arctic Ocean circulation (Rudels et al., 1994). The bathymetry of the Arctic Ocean differs from that in other other oceans in part because of the preponderance of shelf seas, comprising 53% of the total surface area (Jakobsson, 2002). The remaining 47% of the surface area covers 95% of the total volume of the Arctic Ocean, split across four deep basins: the Nansen basin,

5   the Amundsen basin, the Makarov basin, and the Canadian basin. Water masses enter these deep basins (1) via deep inflow from the Atlantic through the Fram Strait into the Nansen basin, (2) via deep-water inflow from the Barents Sea to the Nansen basin through the St Anna Trough, as cooling increases density, (3) and via density flows along the continental shelves that are driven by brine rejection from sea-ice formation (Jones et al., 1995). These three local processes are difficult to resolve in coarse-resolution models, e.g., local density flows necessitate much higher resolution (Proshutinsky et al., 2016). Model

10 resolution also affects the simulated interior circulation of the Arctic Ocean by its connection to the global ocean circulation via four relatively narrow and shallow passages: (1) the Canadian Archipelago, (2) the Fram Strait, (3) the Barents Sea Opening and (4) the Bering Strait (Aksenov et al., 2016). Lateral exchange of water, carbon, and nutrients across these sections also affects Arctic Ocean primary production and acidification (Popova et al., 2013; Luo et al., 2016).

Here we use a three-dimensional model to help refine the estimate of the total anthropogenic carbon in the Arctic Ocean

15 while assessing the dominant pathways by which anthropogenic carbon enters the Arctic Ocean and the relative importance of that lateral input relative to the air-sea flux. Three simulations made at increasingly higher grid resolution allow us to assess the extent to which the coarse resolution used by typical global ocean models may need to be improved to adequately estimate storage of anthropogenic carbon in the Arctic Ocean and associated ocean acidification.

2   Methods

20 ### 2.1   Models

For our study, we use the global ocean circulation model NEMO-v3.2 (Nucleus for European Modeling of the Ocean - version 3.2) including its biogeochemical component PISCES-v1 (Pelagic Interactions Scheme for Carbon and Ecosystem Studies) (Aumont and Bopp, 2006). The NEMO model has three parts: (1) the ocean dynamics and thermodynamics model OPA (Madec, 2008), (2) the sea-ice model LIM (Vancoppenolle et al., 2009), and (3) the passive tracer module TOP. This physical

25 model is coupled via TOP to version 1 of PISCES. In this study we use NEMO at three resolutions: a laminar 2°-configuration (ORCA2) typical of coarse-resolution ocean models (Madec et al., 1998), which does not resolve eddies; an intermediate 0.5°-configuration (ORCA05) that just begins to allow eddies to appear spontaneously (Bourgeois et al., 2016); and a higher-resolution, eddy admitting version, i.e., 0.25°-configuration (ORCA025), which is still not eddy resolving (Barnier et al., 2006). All three configurations have a tripolar, curvilinear horizontal grid. One grid pole (singularity) is located at the geographical

30 South Pole while the conventional North-Pole grid singularity over the Arctic Ocean has been replaced by two singularities, both displaced over land, one over Canada and the other over Russia (Madec et al., 1998), thereby saving computational costs and avoiding numerical artifacts.

From 90°S to 20°N, the grid is a normal Mercator grid; north of 20°N, it is distorted into ellipses to create the two northern singularities (Barnier et al., 2006; Madec, 2008). The grid size changes depending on resolution and location (Table 3). The mean horizontal grid size in the Arctic Ocean (average length of the 4 horizontal edges of surface grid cells in the Arctic Ocean) is 121 km in ORCA2, 29 km in ORCA05, and 14 km in ORCA025. The minimum horizontal grid size in the Arctic is 63 km

5 in ORCA2, 9 km in ORCA05, and 3 km in ORCA025. Vertically, all three model configurations have the same discretization, where the full-depth water column is divided into 46 depths levels, whose thicknesses increase from 6 m at the surface to 500 m in the deepest grid box. For ocean bathymetry, the 2-minute bathymetry file ETOPO2 from the National Geophysical Data Center is used, which is based on satellite derived data (Smith and Sandwell, 1997) except for the highest latitudes: the IBCAO bathymetric data is used in the Arctic (Jakobsson et al., 2000) and BEDMAP bathymetric data is used for the Southern

10 Ocean south of 72°S (Lythe and Vaughan, 2001). To interpolate the bathymetry on the model grid, the median of all data points in one model grid cell was computed. NEMO uses partial steps so that the model better matches the observed topography. Thus the depth of the deepest cell can be smaller than the original grid cell. For the parameter values and numerical characteristics of the ORCA025 configuration, we follow Barnier et al. (2006). The lateral isopycnal diffusion and viscosity coefficients are then chosen depending on the resolution (Table 1). Note that a Laplacian viscosity operator is used in ORCA2, whereas a

15 bi-Laplacian operator is used in ORCA05 and ORCA025. To simulate the effect of eddies on the mean advective transport in the two coarser resolution configurations, the eddy parameterization scheme of Gent and Mcwilliams (1990) was applied with eddy diffusion coefficients indicated in Table 1.

The biogeochemical model PISCES (Aumont and Bopp, 2006) includes four plankton functional types: two phytoplankton (nanophytoplankton and diatoms) and two zooplankton (micro- and meso-zooplankton). The growth of phytoplankton is lim-

20 ited by the availability of five nutrients: nitrate, ammonium, total dissolved inorganic phosphorus P_T, total dissolved silicon Si_T, and iron. The nanophytoplankton and diatoms are distinguished by their need for all nutrients, with only diatoms requiring silicon. In the living compartments, the macronutrient ratios are held constant at C:N:P = 122:16:1 (Takahashi et al., 1985). The same ratio holds for nonliving compartments: dissolved organic matter (DOM) and both small and large sinking particles, which differ in their sinking velocity. In PISCES, nutrients are supplied by three external pathways: atmospheric dust deposi-

25 tion, river delivery, and sediment mobilization. Dust deposition is taken from a simulation by Tegen and Fung (1995). River discharge of C_T and dissolved organic carbon (DOC) is based on the Global Erosion Model (GEM) by Ludwig et al. (1998). Riverine DOC is assumed to be labile, being transformed into C_T as soon as it enters the ocean. River delivery of the other four nutrients (Fe, N, P, and Si) are calculated from C_T, assuming constant ratios of C:N:P:Si:Fe = 320:16:1:53.3:3.64 × 10^{-3} (Meybeck, 1982). For sediment mobilization, dissolved iron input was parameterized as 2 μmol Fe m^{-2} day^{-1} for depths

30 shallower than 1100 m following the lead of Moore et al. (2004).

2.2 Biogeochemical simulations

For initial conditions, we used observational climatologies for temperature and salinity combined from three sources (Barnier et al., 2006), for dissolved oxygen and nutrients (nitrate, P_T, and Si_T) from the 2001 World Ocean Atlas (Conkright et al., 2002), and for preindustrial C_T and A_T from the observation-based Global Data Analysis Product (GLODAP) (Key et al.,

2004). As comparable observational climatologies for DOC and iron are lacking, those variables were initialized from output of a 3000-year spin up of an ORCA2 simulation including PISCES. Other tracers have short recycling times and thus were initalized with globally uniform constants.

For physical boundary conditions, all simulations are forced with the same DRAKKAR Forcing Set (DFS) constructed by Brodeau et al. (2010). This historical reanalysis data set provides surface air temperature and humidity at 2 m, wind fields at 10 m, shortwave and longwave radiation, and the net surface freshwater flux (evaporation minus precipitation). This data set covers 55 years, including 1958–2001 from version 4.2 and then 2002–2012 from version 4.4.

A 50-year spin up was first made from rest in the ORCA05 NEMO-PISCES model (coupled circulation-biogeochemistry), after initializing the model variables with the above-mentioned fields. The resulting simulated physical and biogeochemical fields were then used to initialize the ORCA05 NEMO-PISCES simulations, and that model was subsequently integrated during 1870-1957. Since no atmospheric reanalysis is available during that period, we simply loop the DRAKKAR Forcing Set. Then at the beginning of 1958, the ORCA05 simulated fields were interpolated to the ORCA2 and ORCA025 grids, and simulations were continued in each of the three configurations during 1958 to 2012 (Fig. 1).

For this study we made two types of simulations, historical and control, both forced with the same reanalysis fields. In addition, the control simulation is forced with the preindustrial CO_2 concentration of 287 ppm in the atmosphere over the entire period from 1870 to 2012. The historical simulation is forced with yearly averaged historical atmospheric CO_2 concentrations reconstructed from ice cores and atmospheric records over 1870 to 2012 (Le Quéré et al., 2015). We define the difference between the historical simulation and the control simulation as the anthropogenic component. These ORCA05 simulations were first used by Bourgeois et al. (2016) to assess the budget of anthropogenic carbon in the coastal ocean.

2.3 Perturbation simulation

Because of computational limitations, it was necessary to start the anthropogenic CO_2 perturbation of our reference ORCA05-PISCES simulation in 1870 as opposed to the traditional earlier reference of 1765 (Sarmiento et al., 1992), a more realistic approximation of the start of the industrial-era CO_2 increase. A similar compromise was adopted for CMIP5 (Taylor et al., 2012). During that missing 105 years, atmospheric xCO_2 increased from 277.86 to 287.29 ppm, a 9 ppm difference that seems small relative to today's total perturbation with atmospheric xCO_2 now above 400 ppm. However, Bronselaer et al. (2017) estimated that global ocean uptake of C_{ant} in 1995 is actually underestimated by $\sim$30% (29 Pg C) for simulations that reference the natural preindustrial state to 1850 rather than 1765. The cause is partly due to carbon uptake during the missing 1765–1850 period, but mostly it is due to the higher preindustrial reference for atmospheric xCO_2 that results in the air-sea flux of C_{ant} being underestimated throughout the entire simulation. Unfortunately, we cannot use Bronselaer et al.'s results to correct our biogeochemical simulations because their reference date in the mid 19th century is 20 years earlier than ours and because they do not include the Arctic Ocean in their global data-based assessment.

Instead, to correct results from our biogeochemical simulations, we essentially add in the difference between two additional simulations made in the same circulation model but coupled to the more efficient single-tracer perturbation approach (Sarmiento et al., 1992) rather than the full PISCES biogeochemical model (24 tracers). By definition, the perturbation tracer

is initialized to zero everywhere; it accounts for only the perturbation (C_{ant}), assuming it is independent of the natural carbon cycle. Thus with the same ORCA05 physical configuration, we made two perturbation simulations, one initialized in 1765 (P1765) and the other in 1870 (P1870). Their difference is later added to the NEMO-PISCES simulations.

The perturbation approach of Sarmiento et al. (1992) avoids the computationally intensive standard CO_2 system calculations

5 by focusing only on anthropogenic carbon and exploiting a linear relationship between the anthropogenic change in oceanic pCO_2 and its ratio with the ocean's corresponding change in C_T (C_{ant}):

$$\frac{\delta pCO_{2_{oc}}}{C_{ant}} = z_0 + z_1 \delta pCO_{2_{oc}}, \tag{1}$$

where $\delta pCO_{2_{oc}}$ is the perturbation in oceanic pCO_2 and the coefficients z_0 and z_1 are each quadratic functions of temperature,

$$z_0 = a_0 + a_1 T + a_2 T^2 \tag{2}$$

10 $$z_1 = b_0 + b_1 T + b_2 T^2. \tag{3}$$

In the model, Eq. (1) is rearranged to solve for surface-ocean $\delta pCO_{2_{oc}}$ in terms of C_{ant} (Sarmiento et al., 1992, Eq. (11)), as needed to compute the air-sea flux (Sarmiento et al., 1992, Eq. (2)). In the air-sea flux equation, the atmospheric xCO_2 is corrected for humidity and atmospheric pressure to convert to $pCO_{2_{atm}}$. The atmospheric xCO_2 history for 1765–1869 is from Meinshausen et al. (2017), while the history for 1870 and beyond is the same as used in the NEMO-PISCES simulations.

15 One set of coefficients was derived for our reference atmospheric xCO_2 in 1765; another set was derived for our reference atmospheric xCO_2 in 1870 (Table 2). The original approach was only updated to use the equilibrium constants recommended for best practices (Dickson et al., 2007) and to cover a perturbation of up to 280 ppm (see Supplement). The relative error introduced by approximating the perturbation to the ocean CO_2 system equilibria with Eq. (1) remains less than $\pm 0.3\%$ across the global ocean's observed temperature range when $\delta pCO_2^{oc} < 280$ ppm.

20 To correct our biogeochemical simulations for the late starting date, we use the time-varying difference in C_{ant} for every grid cell between the two perturbation simulations (P1765 − P1870), adding that to the C_{ant} simulated in the biogeochemical simulations. That late-start-date correction is applied to all model output when computing the total C_{ant} inventories and the vertical C_{ant} profiles (Sects. 3.3 and 4.2). On the other hand, that correction is not applied when the focus is on differences between 1960 and 2012 because the correction for that period is small; it is also less certain when applied to results from

25 ORCA2 and ORCA025 given that it is based results from ORCA05. Thus it is not applied when discussing the effects of resolution, the 1960-2012 budget, lateral fluxes, nor changes in the aragonite saturation horizon during that time (Sects. 3.4, 4.3, 4.4, and 4.6). To illustrate the generally second-order effect of this correction on for instance the lateral fluxes of C_{ant}, results from both perturbation simulations are tabulated alongside those from the biogeochemical simulations.

2.4 Arctic Ocean

30 To assess the anthropogenic carbon budget in the Arctic Ocean, we adopted the regional domain defined by Bates and Mathis (2009) (Fig. 2). That domain's lateral boundaries and the volume of water contained within them vary slightly among the three model versions due to their different resolutions and bathymetries. (Table 3). The signature of these different volumes is also

apparent in the integrated quantity of anthropogenic carbon that is stored in the Arctic in 1958, even though the fields for all three models are based on the same 1957 field from the ORCA05 model (Fig. 1).

2.5 Transport across boundaries

Transects were defined (Fig. 2) along the four boundaries as consistently as possible for the three resolutions. Water transport across each of the four boundaries was calculated for each model configuration by using monthly average water velocities at each boundary grid cell along a transect multiplied by the corresponding area of the face of the grid cell through which the water flows. For boundaries defined by a row of cells (Fram Strait, Canadian Arctic Archipelago [CAA], and Bering Strait), the transport was calculated across the northern face of each cell. Conversely, for the boundary that is a jagged line (Barents Sea Opening), for each cell the transport was calculated at the northern and eastern faces of each cell and the two transports are summed. Then for each transect, transport across all of its cells are summed to obtain the transect's monthly net transport. For the C_{ant} transport, we did the same but also multiplied the water transport at the boundary between two grid cells with their volume-weighted monthly-average concentration. This multiplication of monthly means introduces an error into the transport calculation owing to neglect of shorter term variability. To shed light on that error, we summed results from those monthly calculations across all four sections, integrated them over time from 1960 to 2012, and compared that to the net transport of C_{ant} into the Arctic Ocean implied by the inventory change minus the cumulative air-sea flux over the same time period. The inventory of C_{ant} is the total mass of C_{ant} inside the Arctic Ocean at a given time, while the cumulative flux is the time-integrated air-sea flux of anthropogenic CO_2 over the Arctic Ocean since the beginning of the simulation. The difference between these two spatially integrated values is the reference value for the net lateral flux into the Arctic Ocean to which is compared the less exact total lateral flux of anthropogenic carbon computed from monthly mean velocity and concentration fields integrated over time. The relative error introduced by the monthly average calculations is 27% for ORCA2, 7% for ORCA05, and 4% for ORCA025.

2.6 CFC-12 observational data

Model simulations were evaluated indirectly by comparing simulated to observed CFC-12. We choose CFC-12 to evaluate the model, because it is an anthropogenic, passive, conservative, and inert tracer, and in contrast to anthropogenic carbon, it is directly measurable. The CFC-12 atmospheric concentration increased from zero in the 1930s to its peak in the 2000s, since declining as a result of the Montreal protocol. Thus CFC-12 is a transient tracer similar to anthropogenic carbon but for which there exist extensive direct measurements, all carried out with high precision during WOCE (World Ocean Circulation Experiment) and CLIVAR (Climate and Ocean - Variability, Predictability and Change) era. Nowadays, ocean models are often evaluated with CFC-11 or CFC-12, especially those destined to be used to assess anthropogenic carbon uptake (Dutay et al., 2002; Orr et al., 2017).

The CFC-12 observations used in this study come from two trans-Arctic cruises: the 1994 Arctic Ocean Section (AOS94) (Jones et al., 2007) and the Beringia 2005 expedition (Anderson et al., 2011) (Fig. 2). AOS94 started on 24 July and finished on 1 September, during which CFC-12 measurements were made at 39 stations. That section starts in the Bering Strait, enters

the Canada basin adjacent to Mendeleev ridge, continues to the Makarov basin, and ends at the boundary of the Nansen basin and the Barents Sea. The Beringia expedition started on 19 August and ended on 25 September 2005. It started off the coast of Alaska, went through the Canada and Makarov basins, crossed the Lomonosov ridge, and its last CFC-12 station was taken on the Gakkel ridge. These two cruises were chosen among other cruises because of their geographically similar placement and because they cross large parts of the Arctic, including almost all four major basins.

2.7 Data-based estimates of anthropogenic carbon

Our simulated C_{ant} was compared to data-based estimates from Tanhua et al. (2009) for the year 2005 and from GLODAPv2 for the year 2002 (Lauvset et al., 2016), both based on the TTD approach.

3 Results

3.1 Physical Evaluation

3.1.1 Lateral water fluxes

The lateral water flux across each the four Arctic boundaries is a fundamental reference for the simulated physical transport, especially when the goal is to construct a budget that includes lateral transport of passive tracers. Results for lateral water transport in the three model resolutions may be grouped into two classes: coarse resolution and higher resolutions. In ORCA2, water enters the Arctic Ocean from Barents Sea and the Bering Strait (2.1 Sv split evenly), with 86% of that total leaving the Arctic via the Fram Strait and the remaining 14% flowing out via the CAA (Table 4). Conversely, outflow through the CAA is seven times larger for ORCA05 and nine times larger for ORCA025, being fueled by 26% to 46% more inflow via the Bering Strait and 110% to 170% more inflow via the Barents Sea. Outflow via the Fram Strait is 1.76 Sv in ORCA2, 1.42–1.75 Sv in ORCA05, and 1.46–1.80 Sv in ORCA025, depending on the time period (Table 4).

Relative to the observed CAA outflow of 2.7 Sv (Curry et al., 2014; Straneo and Saucier, 2008), only ORCA05 and ORCA025 simulate similar results. In contrast, ORCA2's simulated CAA outflow is about one ninth of that observed. Likewise, its inflow via the Barents Sea is half of that observed, while the two higher resolution simulations have Barents Sea inflows that are 20% and 40% larger than observed. Yet for inflow through the Bering Strait, it is ORCA2 that is closest to the observed estimate, overestimating it by 30%, while ORCA05 and ORCA025 overestimate it by 60% and 90%. Thus too much Pacific water appears to be entering the Arctic Ocean. All resolutions underestimate the central observational estimate for the Fram Strait outflow by ∼12% but still easily fall within the large associated uncertainty range. Summing up, the net water transport across all four boundaries is not zero. A net outflow between 0.12 and 0.17 Sv is found for the three model resolutions owing to river inflow and precipitation as well as artifacts caused by using monthly averages. In contrast, when the observed water transport estimates at all four boundaries are summed up, there is a net outflow of 1.9 Sv, more than ten times larger. This strong net outflow is also much larger than freshwater input from rivers (0.08 Sv) (McClelland et al., 2006) and precipitation (0.12 Sv) (Yang, 1999). It can only be explained by uncertainties in the data-based estimates of water transport,

which are at least ± 2.7 Sv for the net transport based on the limited uncertainties available for transport across the individual boundaries (Table 4). The excessive central observational estimated for the net outflow might be explained by a data-based estimate for the Barents Sea inflow that is too weak combined with a data-based estimate for the Fram Strait outflow that is too strong, a possibility that is consistent with results from the higher resolution models ORCA05 and ORCA025.

5 ### 3.1.2 Sea ice

Because sea-ice cover affects the air-sea CO_2 flux and hence anthropogenic carbon concentrations in the ocean, we compare the modeled sea-ice cover to that observed by the U.S. National Snow and Ice Data Center (Walsh et al., 2015). Yearly averages of sea-ice extent are quite similar between the observations and models. Only in summer are simulated sea-ice concentrations slightly too high (by 0.25–0.5×10^6 km^3). Despite this overall agreement in integrated sea-ice extent, regional differences are

10 larger. During winter (Fig. 3), all three model configurations marginally overestimate the sea-ice extent northeast of Iceland and north of the Labrador Sea, while the simulated sea-ice extent in the Barents Sea and the Bering Strait are similar to observations. During summer, the simulated sea-ice extent resembles that observed in the eastern Arctic particularly near the Atlantic, but all model resolutions overestimate sea-ice extent north of the Kara Sea, the Laptev Sea, and the East Siberian Sea. This overestimation should reduce air-sea CO_2 fluxes locally in these regions. The close model-data agreement for sea-ice

15 extent in terms of the total amount, its trend and seasonal coverage, as well as regional coverage in winter contrasts with the tendency of the models to overpredict sea-ice cover in summer in the highest latitudes of the eastern Arctic.

3.1.3 Atlantic water

In the Arctic Ocean, water temperature is used to help identify water masses, with values above 0°C typically coming from the Atlantic Ocean (Woodgate, 2013). The observed temperature along the 1994 and 2005 sections (Fig. 4) indicates that Atlantic

20 Water (AW) is found between 200 and 1000 m, penetrating laterally below the strongly stratified Arctic Ocean surface waters. In ORCA025, this AW layer is deeper and more diffuse, lying between 500 and 1500 m, thus leading to a cold bias around 500 m and a warm bias around 1000 m. The Beringia station at the boundary between the Barents Sea and the Nansen basin indicates AW lies between 200 m (2.5°C) and the seafloor at 1000 m (0°C). Conversely in the same location in ORCA025, model temperatures remain above 1.5°C throughout the water column. That lower maximum temperature and weaker vertical

25 gradient suggests that when ORCA025's Atlantic water enters the Arctic Ocean through the Barents Sea it is too diffuse, being well mixed throughout the water column. Weaker maxima in the simulated temperature relative to observations are also found further west in the Canada basin along both sections. There observed temperatures reach maxima of 1.1°C, while ORCA025's maxima reach only 0.5°C.

The other two resolutions represent Atlantic water circulation more poorly than does ORCA025. Both simulations show

30 water with temperatures higher than 0°C only at the southern end of the Nansen basin. Vertically, these water masses are situated around 400 m for ORCA2 and between 200 and 1300 m for ORCA05.

3.2 CFC-12

Simulated CFC-12 was compared among the three resolutions and with observations, focusing first on basin-scale tendencies based on vertical profiles of the distance-weighted means along the 2005 section (Fig. 5). That comparison reveals that among resolutions, simulated CFC-12 concentrations differ most between 400 m and 2000 m; conversely, simulated average profiles

5 are nearly insensitive to resolution both above and below that intermediate zone. In those intermediate waters and above, simulated concentrations are also generally lower than observed. The only exceptions are (1) the top 100 m of the Canada basin where all resolutions overestimate observed values by 10% and (2) between 1000 and 2000 m in the Canada and Makarov basins where the ORCA025 model overpredicts observations by up to 40%. Conversely, lower resolution generally implies lower and less realistic simulated CFC-12 concentrations in the intermediate zone. Below 2000 m, the simulated concentrations

10 are essentially zero, while the observations are only slightly higher (0.12 pmol kg^{-1}). For comparison, the reported detection limit for CFC-12 for the Beringia 2005 expedition is 0.02 pmol kg^{-1} (Anderson et al., 2011). The general shape of profiles also differs. While the observations exhibit a generally smooth decline down to about 1500 m, the models show a steeper reduction down to about 300 m and then much weaker gradients down to 1500 m. While ORCA2 tends to decline quickly at first, ORCA05 generally remains nearly vertical, and ORCA025 actually even increases with depth in the Canada and Makarov

15 basins.

Given the closer overall agreement of the ORCA025 CFC-12 simulation with observations, let us zoom in to compare its details to observations along the 1994 and 2005 sections (Fig. 6). On the Atlantic end of the Beringia 2005 section, where water enters the Nansen basin from the Barents Sea, the water column in ORCA025 appears too well mixed, having CFC-12 concentrations that remain above 2.0 pmol kg^{-1}. Conversely, observed CFC-12 is less uniform, varying from 2.8 pmol kg^{-1} at the

20 surface to 1.3 pmol kg^{-1} in bottom waters at 1000 m, thereby indicating greater stratification. The same contrast in stratification was deduced from modeled and observed temperature profiles at the same location (Sect. 3.1.3). On the other side of the Arctic in the Canada basin, there are observed local chimneys of CFC-12 where concentrations remain at about 2.0 pmol kg^{-1} from near the surface down to 1000 m, particularly in the 1994 section. These chimneys suggest localized mixing that is only barely apparent in ORCA025 6). Such localized features are absent at lower resolution.

25 ## 3.3 Anthropogenic carbon inventories and concentrations

The globally integrated increase in C$_{ant}$ due to an earlier start date, as assessed with our two perturbation simulations (P1765 – P1870), is 24 Pg C in 1995, an adjustment to the global inventory that is 17% lower than Bronselaer et al.'s data-based assessment for a 1765 vs. 1850 start date. In the Arctic Ocean, which is absent from the data-based assessment, there was a corresponding simulated basin-wide increase of 0.4 Pg C in 2005.

30 The simulated basin-wide storage (inventory) of simulated C$_{ant}$, adjusted for the late starting date, was compared to the TTD-based estimates of anthropogenic carbon from (1) the GLODAPv2 assessment (Lauvset et al., 2016) normalized to the year 2002 and (2) the Tanhua et al. (2009) assessment normalized to 2005. These data-based estimates suggest that 2.9 Pg C of anthropogenic carbon was stored in the Arctic Ocean in 2002 while 2.5–3.3 Pg C was stored there in 2005. The adjusted

modeled C_{ant} inventory in 2002 ranges from 1.9 to 2.5 Pg C (from ORCA2 to ORCA025), the upper end of which remains 0.4 Pg C lower than the GLODAPv2 data-based estimate. In 2005, the modeled range is slightly higher (2.0 to 2.6 Pg C) with the upper end from ORCA025 falling just within the data-based uncertainty range of Tanhua et al. (2009).

These model-data differences in basin-wide inventories were investigated further by comparing vertical profiles of C_{ant} from
5 the models to those from the GLODAPv2 data-based estimates (Fig. 7). Surface concentrations in ORCA05 and ORCA025 are up ~35% larger (+12 µmol kg⁻¹) than the data-based estimate, whereas the ORCA2 concentration is ~22% larger (+7 µmol kg⁻¹). Diving deeper, by 150 m the simulated concentrations in all resolutions drop below the data-based estimates and remain so, except for ORCA025, down to the ocean bottom. At 400 m the difference is largest, with all resolutions underestimating data-based estimates by up to ~28% (9 µmol kg⁻¹). Below 400 m, results from the three resolutions differ
10 more. The ORCA2 C_{ant} concentration decreases monotonically to 11 µmol kg⁻¹ at 1000 m and to 0 µmol kg⁻¹ at 2300 m. In ORCA05, concentrations decrease slowly to 19 µmol kg⁻¹ at 1000 m, below which they decrease rapidly, essentially to 0 µmol kg⁻¹ at 2300 m. Only ORCA025 increases again below 400 m, reaching a local maximum in C_{ant} at 900 m, an increase that causes the ORCA025 results to exceed data-based estimates by up to 2 µmol kg⁻¹ (~11%) at 1100 m. Below 1500 m, ORCA025 concentrations decline quickly, essentially reaching zero at 2300 m. Conversely, data-based anthropogenic carbon
15 concentrations remain at roughly a constant 6 µmol kg⁻¹ all the way down to the seafloor. The main differences between ORCA025 and data-based estimates are thus found in the deep Arctic Ocean below 1600 m. An analogous simulated local maximum and the underestimation near 400 m was also seen for CFC-12 (Fig. 5). Unlike for C_{ant} though, CFC-12 results differ below 2000 m, where observed CFC-12 concentrations are proportionally much smaller than those above.

3.4 Anthropogenic carbon budget

20 We calculated the budget for C_{ant} from 1960 to 2012 (Tables 4 and 5). During this period, the C_{ant} inventory in ORCA025 increased by 1.91 Pg C, 80% of which is stored in the four major Arctic Oceans basins: the Nansen Basin (0.29 Pg C), the Amundsen Basin (0.33 Pg C), the Makarov Basin (0.32 Pg C) and the Canada Basin (0.57 Pg C). Although the Canada Basin C_{ant} inventory increased most, its volume is larger so that its average C_{ant} concentration increased less than in the other basins (Fig. 7). Out of the total inventory stored in the Arctic Ocean during these five decades, about one-fourth (0.47 Pg C)
25 entered the Arctic Ocean via air-sea flux, most of which was transferred from atmosphere through the surface of the Barents Sea (Fig. 8). The remaining 75% (1.45 Pg C) entered the Arctic Ocean via lateral transport. This net lateral influx is the sum of the fluxes (1) from the Atlantic through the Fram Strait (0.04 Pg C), (2) from the Atlantic to the Barents Sea (1.70 Pg C), (3) from the Pacific through the Bering Strait (0.89 Pg C) and (4) to the Atlantic via the CAA (-1.25 Pg C). Summed up, the net inflow across the four boundaries is 1.39 Pg C. This lateral flux computed from monthly mean C_{ant} concentrations and flow
30 fields is 0.06 Pg C (~4%) smaller than the lateral flux computed from the change in inventory minus the cumulative air-sea flux (Fig. 8). Within the Arctic, coastal regions typically exhibit net lateral losses, while the deep basins exhibit net lateral gain. The largest lateral loss occurs in the Barents Sea, where the cumulative air-sea flux of C_{ant} is also largest (Fig. 8).

The budget of C_{ant} changes notably with resolution. Higher resolution results in more simulated C_{ant} being stored in the Arctic region, with increases in both the cumulative air-sea flux and lateral transport. The C_{ant} inventory change from 1960

to 2012 nearly doubles with the resolution increase between ORCA2 and ORCA025 (from 1.04 to 1.91 Pg C). Out of that additional C_{ant}, 93% is found between 300 and 2200 m with the maximum being located at 1140 m. The remaining 7% is located between the surface and 300 m (Fig. 7). Besides these differences in the vertical partitioning of stored C_{ant}, resolution also affects regional partitioning of C_{ant} (Figs. 7 and 8). When refining resolution from ORCA2 to ORCA05, the Arctic Ocean

5 C_{ant} inventory increases by 0.46 Pg C, 72% of which occurs in the two Eurasian basins: the Nansen (0.19 Pg C) and Amundsen (0.14 Pg C) basins. Another 24% of that increase occurs in the two Amerasian basins: the Makarov (0.06 Pg C) and Canada (0.05 Pg C) basins. Coastal regions account for only 4% of the total inventory increase. In contrast, the subsequent resolution enhancement between ORCA05 and ORCA025 results in little increase in inventory in the Eurasian basins (0.02 Pg C) but much more in the Amerasian basins (0.35 Pg C).

10   As resolution is refined between ORCA2 and ORCA025, the Arctic C_{ant} inventory increases as a result of a 62% increase in the air-sea flux (+0.18 Pg C) and a 93% increase in the lateral flux (+0.70 Pg C). Thus the relative contribution of the lateral flux increases from 72% to 76%. Changing model resolution also affects the pathways by which C_{ant} enters the Arctic Ocean (Table 4). The most prominent change occurs in the CAA. From ORCA2 to ORCA025 the net outflow of C_{ant} through the CAA increases sevenfold (from -0.18 to -1.25 Pg C). Other notable changes include (1) the net transport through the Fram

15 Strait declining from a sizable net outflow (-0.59 Pg C) to a slight net inflow (0.04 Pg C), (2) the inflow through the Barents Sea increasing by 150% (from 0.68 to 1.70 Pg C), and (3) the inflow of C_{ant} through the Bering Strait increasing by 40% (from 0.64 to 0.89 Pg C).

4   Discussion

4.1   CFC-12

20 The simulated CFC-12 in ORCA025 underestimates observed concentrations between 100 and 1000 m, overestimates them between 1000 and 2000 m, and closely matches the low observed concentrations below 2000 m. Temperature sections suggest that that excess simulated CFC-12 between 1000 and 2000 m is due to a vertical displacement of inflowing Atlantic water, which descends too deeply into the Arctic (Fig. 4). Such vertical displacement would indeed reduce simulated CFC-12 concentrations above 1000 m and enhance them between 1000 and 2000 m. Yet the underestimation of integrated CFC-12 mass

25 above 1000 m is larger than the overestimation below 1000 m. Thus vertical displacement of Atlantic water cannot provide a full explanation. Simulated CFC-12 concentrations above 1000 m could also be too low because ventilation of subsurface waters is too weak, an hypothesis that is consistent with the simulated vertical gradients in both temperature and CFC-12 that are too strong between 100 and 1000 m.

4.2   Anthropogenic carbon

30 Relative to CFC-12, simulated deep C_{ant} in ORCA025 underestimates observational estimates of C_{ant} by proportionally much more. Both tracers have similarly shaped profiles, but the data-based C_{ant} profile differs from observed CFC-12 below 1500 m.

Above 1000 m, ORCA025 underestimates data-based estimates of C_{ant} as well as observed CFC-12 owing to weak ventilation in the model. Between 1000 and 2000 m, simulated C_{ant} and CFC-12 in ORCA025 are higher than data-based and observed concentrations. The local maxima for simulated CFC-12 and C_{ant} in that depth range can be explained by the excessively deep penetration of simulated Atlantic water masses, which are rich in both tracers.

5   Below 1500 m, simulated C_{ant} largely underestimates data-based estimates. These data-based C_{ant} concentrations remain higher than those simulated, with an offset of $\sim$6 μmol kg^{-1} from 2000 m to the ocean floor (amounting to 18% of the surface concentration), while observed CFC-12 concentrations are close to those simulated, dropping to 0.1 pmol kg^{-1} below 2000 m (amounting to 3% of the surface concentration). Hence the data-based estimates of C_{ant}, which are not measured directly, appear to be too large below 1500 m in the Arctic Ocean. Below 2000 m, assuming that the actual concentrations

10   of C_{ant} remain close to zero as suggested by the observed distribution of CFC-12, we can roughly estimate the effect on the basin-wide inventory by zeroing out those concentrations in the GLODAPv2 estimates (Lauvset et al., 2016) and recomputing the inventory. Doing so reduces the data-based inventory in 2002 by 10%. Applying the same 10% relative decrease to both limits of the data-based range from Tanhua et al. (2009) reduces that to 2.2–3.0 Pg C. That modified range brackets simulated inventories from both ORCA05 and ORCA025.

15   ## 4.3   Lateral flux

In our model, about three-fourths of the net total mass of C_{ant} that accumulates in the Arctic Ocean enters laterally from the Atlantic and Pacific Oceans, independent of model resolution. Our simulated lateral fluxes of C_{ant} were compared to data-based estimates from studies that multiply C_{ant} concentrations (TTD data-based estimates) along the Arctic boundaries by corresponding observation-based estimates of water transport.

20   The simulated lateral transport of C_{ant} in ORCA025 generally agrees with data-based estimates within the latter's large uncertainties. These uncertainties result from uncertainties in data-based estimates of C_{ant} and from uncertainties in observational constraints on water flow, which also varies interannually (Jeansson et al., 2011). For the Fram Strait, Jeansson et al. (2011) estimated a net C_{ant} outflux (from the Arctic) of 1 ± 17 Tg C yr^{-1} in 2002, while for 2012 Stöven et al. (2016) estimate an outflux of 12 Tg C yr^{-1} but without uncertainties. For the same years, ORCA025 simulates a net outflux of 6 Tg C yr^{-1}

25   in 2002 but a net influx (to the Arctic) of 7 Tg C yr^{-1} in 2012. Both model and data-based estimates vary greatly between 2002 and 2012. Across the Barents Sea Opening, there is a consistent net influx from the Atlantic to the Arctic Ocean, i.e., 41 ± 8 Tg C yr^{-1} in 2002 for the data-based estimate (Jeansson et al., 2011) and (44 Tg C yr^{-1}) for ORCA025.

More recently, Olsen et al. (2015) added data-based estimates of lateral fluxes at the two other major Arctic Ocean boundaries, completing the set of four that define the perimeter. They estimate an inflow of $\sim$18 Tg C yr^{-1} from the Pacific

30   through the Bering Strait and an outflow through the CAA of $\sim$29 Tg C yr^{-1}, both for the 2000s. For the same time period, ORCA025 simulates one-third more inflow through the Bering Strait ($\sim$24 Tg C yr^{-1}) and 7% more outflow through the CAA ($\sim$31 Tg C yr^{-1}). The larger Bering-Strait C_{ant} inflow in ORCA025 is consistent with its overestimated Bering-Strait water inflow (Table 4, Section 3.1.1). Integrating over all four lateral boundaries, Olsen et al. found a total net C_{ant} influx of $\sim$29 Tg C yr^{-1}, which is 22% less than that simulated in ORCA025 ($\sim$37 Tg C yr^{-1}). Olsen et al. did not provide uncertain-

ties, but the uncertainty of their net lateral flux estimate is at least ± 18 Tg C yr^{-1} based on the data-based transport estimates at the two other Arctic boundary sections where uncertainties are available (Table 4).

Although the simulated and data-based lateral fluxes generally agree within available uncertainties, results for the former are not corrected for the 1870 start date of the biogeochemical simulations. Correcting to a 1765 start date would increase the

5   magnitude of the simulated lateral fluxes by 10% to 20% based on our ORCA05 perturbation simulations (compare P1765 to P1870 in Table 5). However, that correction may depend on resolution. In any case, we expect it will remain much smaller than the differences due to resolution.

Weighing in at about one-third of the lateral flux is the simulated air-sea flux of C_{ant} in ORCA025 of 10 Tg C yr^{-1} in 2005. That simulated estimate is only about 40% of the data-based estimate of 26 Tg C yr^{-1} from Olsen et al. (2015). Although no

10 uncertainty is provided with that data-based air-sea flux estimate, it too must be at least ± 18 Tg C yr^{-1} given that it is calculated as the difference between the data-based storage estimate (Tanhua et al., 2009) and Olsen et al.'s data-based net lateral flux. Given that large uncertainty, the modeled and data-based estimates of the air-sea flux are not statistically different. In any case, both the model and data-based estimates suggest that the air-sea flux plays a minor role in the anthropogenic carbon budget of the Arctic Ocean, respectively representing 24 and 47% of the total C_{ant} input. For both, the lateral flux dominates.

15 **4.4 Model Resolution**

Basin inventories of anthropogenic carbon differ because of how resolution affects their volume, bathymetry, circulation patterns, and source waters. Much of the water in the Nansen and Amundsen basins has entered laterally from the Atlantic Ocean through the Fram Strait and the Barents Sea (Jones et al., 1995). Water inflow through the Barents Sea increases by 150% when changing from ORCA2 to ORCA05 but only by 20% more between ORCA05 and ORCA025. Water inflow in those two

20 higher resolution models is also closer to observational estimates. Furthermore, the larger lateral water fluxes in ORCA05 and ORCA025 largely explain their higher C_{ant} concentrations in the Nansen and Amundsen basins. Some of this inflowing water continues to flow further along the slope, across the Lomonosov ridge into the Makarov basin, and then across the Mendeleev ridge into the Canada basin. Yet how well models simulate that flow path depends on lateral resolution. Between ORCA2 and ORCA05, basin C_{ant} inventories increase by 17% in the Canada basin (+0.05 Pg C) and by 43% the Makarov basin

25 (+0.06 Pg C). But between ORCA05 to ORCA025, increases are two to four times greater: +0.23 Pg C in the Canada basin and +0.12 Pg C in the Makarov basin (Sect. 3.4).

As this increase stems from finer, more realistic representation of lateral transport within the Arctic, it would appear that eddying ocean models may be needed to adequately simulate the interior circulation in terms of its effect on C_{ant} storage in the Arctic Ocean. In the Canada basin though, such lateral inflow may not be the only source of C_{ant}. Another major source

30 appears to come from density flows along the continental slope, driven by brine rejection from sea-ice formation over the continental shelves (Jones et al., 1995). A signature of this source in the observed sections may be the chimneys of constant CFC-12 concentration from the surface to about 1000 m in the Canada basin, features for which only ORCA025 exhibits any such signature, albeit faint. To adequately model lateral fluxes of C_{ant} in the Arctic Ocean, at least a resolution comparable

14

to that used in ORCA05 may be needed, while resolutions comparable to that in ORCA025 or above may well be required to begin to capture the effects from density flows along the slope.

4.5 CMIP5 comparison

For wider perspective, we compared the forced NEMO-PISCES simulations to nine ocean biogeochemical models that were coupled within different earth system modeling frameworks as part of CMIP5 (Fig. 9). When the CMIP5 models are compared to the corrected data-based estimate of the C_{ant} inventory (Sect. 4.2), only the MIROC-ESM and NorESM1-ME models with their inventories of 2.7 Pg C and 2.4 Pg C fall within our simplistic revision of the data-based uncertainty estimate (2.2 to 3.0 Pg C in 2005). Nearby though is the HadGEM2-ES, which falls below the lower limit by 0.2 Pg C. Further off are the MPI-ESM and GFDL-ESM models with their C_{ant} inventories in 2005 that are 0.6 to 1.2 Pg C lower than the lower limit. The lowest estimates though are from both versions of the IPSL model whose inventories reach only 25% of the lower limit of our revised data-based range. Adjusting the CMIP5-model Arctic inventories upward by ∼0.4 Pg C to account for their late start date in 1850, as we did for our three simulations, would place three of them (MIROC-ESM, NorESM1-ME, and HadGEM2-ES) above the lower boundary of our revised data-based uncertainty estimate. For the cumulative air-sea flux between 1960 and 2012, for which there is no data-based constraint, all models fall between 0.3 and 1.2 Pg C. Lateral fluxes also vary between models, from an outflow of 0.3 Pg C in the IPSL-CM5A-LR model and an inflow of 1.1 Pg C in the MIROC-ESM model. Only the first three CMIP5 models mentioned above exhibit large net inflow of C_{ant} into the Arctic basin (between 0.7 and 1.1 Pg C from 1960–2012), a condition that appears necessary to allow a model to approach the estimated data-based inventory range. Indeed, the six other CMIP5 models have lower lateral fluxes (-0.5 to 0.5 Pg C) and simulate low C_{ant} storage in 2005.

What is perhaps most surprising are the large differences between our forced ORCA2 model and the IPSL-CM5A-LR and IPSL-CM5A-MR ESMs. All three of those models use ORCA2, although both ESMs rely on an earlier version with a different vertical resolution (31 instead of 46 vertical levels). That contrast in vertical resolution may explain part of the large differences in inventory (1.5 Pg C for our forced version vs. 0.3–0.6 Pg C for the two coupled versions) but the forcing and different model parameters could just as well be responsible. Thus lateral resolution is not the only factor when aiming to provide realistic simulations of C_{ant} storage and lateral transport in the Arctic. Sensitivity studies testing other potentially critical factors are clearly merited.

4.6 Effect on aragonite saturation state

Given that C_{ant} is affected by lateral model resolution, so must be ocean acidification. The aragonite saturation state (Ω_A) was computed for each resolution from the historical run's C_T, A_T, T, S, P_T, and Si_T, after correcting C_T and A_T for drift based on the control run. The higher concentrations of C_{ant} in the ORCA05 and ORCA025 simulations reduces Ω_A between 1960 and 2012 by more than twice as much as found with the ORCA2 model during the same period (Fig. 10). These differences translate into different rates of shoaling for the aragonite saturation horizon (ASH), i.e., the depth where $\Omega_A = 1$. During 1960–2012, the ASH shoals by ∼50 m in ORCA2, while it shoals by ∼150 m in ORCA05 and ∼210 m in ORCA025. Thus model resolution also affects the time at which waters become undersaturated with respect to aragonite.

Although basin-wide mean surface Ω_A does not differ among resolutions, there are regional differences such as over the Siberian shelf (Fig. 11). While the minimum Ω_A in that region reaches 0.9 in ORCA2, it drops to 0.4 in ORCA05 and 0.1 in ORCA025. That lower value in ORCA025 is more like that observed, e.g., down to 0.01 in the Laptev Sea (Semiletov et al., 2016). As these low extremes in Ω_A are extremely local, they cannot be expected to be captured in coarse-resolution models
5 (ORCA2). Higher-resolution models are needed in the Arctic to assess local extremes not only in terms of ocean acidification but also other biogeochemical variables.

5 Conclusions

Global-ocean biogeochemical model simulations typically have coarse resolution and tend to underestimate the mass of C_{ant} stored in the Arctic Ocean. Our sensitivity tests suggest that more realistic results are offered by higher-resolution model
10 configurations that begin to explicitly resolve ocean eddies. Our highest resolution model falls within the uncertainty range of Tanhua et al. (2009)'s data-based estimate for C_{ant} storage in the Arctic Ocean (2.5–3.3 Pg C in 2005). Yet that data-based range may need to be adjusted downward. Data-based C_{ant} concentrations below 2000 m remain at about 6 $\mu mol\,kg^{-1}$, while observed CFC-12 concentrations upon which they are based are close to negligible, being proportionally much smaller relative to near-surface concentrations. Zeroing out the C_{ant} concentrations below 2000 m in the GLODAPv2 climatology (Lauvset
15 et al., 2016) reduces the data-based estimates for Arctic Ocean C_{ant} storage by 10% to 2.2–3.0 Pg C in 2005. That revised range encompasses the adjusted simulated basin-wide inventories from the two higher resolutions, ORCA05 and ORCA025 (2.4 and 2.6 Pg C). Details differ though, e.g., with the ORCA025 results underestimating C_{ant} data-based estimates at around 400 m and overestimating them at around 800 m. That deeper model overestimate appears due to excessive penetration of C_{ant}-rich Atlantic water. The shallower model underestimate may be due to inadequate representation of ventilation of intermediate
20 waters via down-slope flows that are driven by brine formation over the Arctic's enormous continental shelf, a transport process that is notoriously difficult to represent in z-coordinate models, especially at lower resolution.

Data-based estimates of C_{ant} in the Arctic Ocean might be improved by testing the TTD method in the model, using the same approach but with modeled CFC-12 and temperature and then comparing the resulting calculated C_{ant} to the directly simulated C_{ant}. With a series of those calculations, the parameters of the TTD approach (Δ/Γ) could be varied and the best
25 ratio selected for the closest match between calculated and simulated C_{ant}. Then that chosen ratio could be applied to the observed CFC-12 rather than using the default ratio of $\Delta/\Gamma = 1$. We leave this effort for future work.

Our forced ocean simulations suggest that Arctic Ocean storage of C_{ant} is driven mostly by net lateral inflow, the total input of which is about three times that from the air-sea flux. That 3:1 ratio varies little with resolution because the lateral flux and the air-sea flux both increase as resolution is refined. Lateral fluxes in the CMIP5 models are generally less dominant but are
30 also highly inconsistent both in magnitude and in the lateral:air-sea flux ratio. Some CMIP5 models even simulate net lateral outflow of C_{ant} and unrealistically low C_{ant} inventories. The only CMIP5 models that succeed in reaching the lower limit of the data-based C_{ant} inventory range are those that have a large net lateral input. The causes of the CMIP5 model differences remain unclear as is often the case when comparing models having many differences. We expect that most of the CMIP5

models have not been evaluated in terms of their ability to simulate realistic lateral water transport at the boundaries of the Arctic Ocean, which is fundamental to simulating realistic C_{ant} but may be problematic given their coarse resolution. The next phase of CMIP (CMIP6) plans to include CFC-12 and related transient transient tracers, which will help weigh simulated results for C_{ant}.

5   As the mass of simulated anthropogenic carbon in the Arctic Ocean increases with resolution, so does the simulated acidification. For instance, during 1960–2012, the average ASH in the Arctic shoals four times faster in ORCA025 than in ORCA2. Higher resolution is also needed to capture local extremes. Although higher horizontal resolution appears necessary to improve future projections of Arctic Ocean acidification, the computational costs of centennial-scale, high-resolution, biogeochemical ocean simulations remain prohibitive. More practical in the short term would be to assess effects from less-costly model im-

10   provements, including heightened vertical resolution, subgrid-scale parameterizations, and adjustments to model parameters for viscosity and slip conditions.

Code availability.   The code for the NEMO ocean model version 3.2 is available under CeCILL license at http://www.nemo-ocean.eu.

Competing interests.   The authors declare that there are not competing interests.

References

Aksenov, Y., Karcher, M., Proshutinsky, A., Gerdes, R., De Cuevas, B., Golubeva, E., Kauker, F., Nguyen, A. T., Platov, G. A., Wadley, M., et al.: Arctic pathways of Pacific Water: Arctic Ocean model intercomparison experiments, J. Geophys. Res. Oceans, 121, 27–59, doi:10.1002/2015JC011299, 2016.

5 Anderson, L., Tanhua, T., Jones, E., and Karlqvist, A.: Hydrographic, chemical and carbon dioxide data from R/V Oden cruise 77DN20050819, August 19 - September 25, 2005, doi:10.3334/CDIAC/otg.CLIVAR_77DN20050819, 2011.

Aumont, O. and Bopp, L.: Globalizing results from ocean in situ iron fertilization studies, Global Biogeochem. Cycles, 20, doi:10.1029/2005GB002591, 2006.

Barnier, B., Madec, G., Penduff, T., Molines, J.-M., Treguier, A.-M., Le Sommer, J., Beckmann, A., Biastoch, A., Böning, C., Dengg, J.,

10 et al.: Impact of partial steps and momentum advection schemes in a global ocean circulation model at eddy-permitting resolution, Ocean Dyn., 56, 543–567, doi:10.1007/s10236-006-0082-1, 2006.

Bates, N. and Mathis, J.: The Arctic Ocean marine carbon cycle: evaluation of air-sea CO_2 exchanges, ocean acidification impacts and potential feedbacks, Biogeosciences, 6, 2433–2459, doi:10.5194/bg-6-2433-2009, 2009.

Bekryaev, R. V., Polyakov, I. V., and Alexeev, V. A.: Role of polar amplification in long-term surface air temperature variations and modern

15 Arctic warming, J. Clim., 23, 3888–3906, doi:10.1175/2010JCLI3297.1, 2010.

Bourgeois, T., Orr, J. C., Resplandy, L., Terhaar, J., Ethé, C., Gehlen, M., and Bopp, L.: Coastal-ocean uptake of anthropogenic carbon, Biogeosciences, 13, 4167–4185, doi:10.5194/bg-13-4167-2016, 2016.

Brewer, P. G.: Direct observation of the oceanic CO2 increase, Geophys. Res. Lett., 5, 997–1000, doi:10.1029/GL005i012p00997, 1978.

Brodeau, L., Barnier, B., Treguier, A.-M., Penduff, T., and Gulev, S.: An ERA40-based atmospheric forcing for global ocean circulation

20 models, Ocean Model., 31, 88–104, doi:10.1016/j.ocemod.2009.10.005, 2010.

Broecker, W., Takahashi, T., and Peng, T.: Reconstruction of past atmospheric CO_2 contents from the chemistry of the contemporary ocean: an evaluation, Tech. Rep. DOE/OR-857, US Department of Energy, Washington DC, 1985.

Bronselaer, B., Winton, M., Russell, J., Sabine, C. L., and Khatiwala, S.: Agreement of CMIP5 Simulated and Observed Ocean Anthropogenic CO2 Uptake, Geophys. Res. Lett., 44, 12,298–12,305, doi:10.1002/2017GL074435, 2017.

25 Chen, G.-T. and Millero, F. J.: Gradual increase of oceanic CO2, Nature, 277, 205–206, doi:10.1038/277205a0, 1979.

Conkright, M. E., Garcia, H. E., O'Brien, T. D., Locarnini, R. A., Boyer, T. P., Stephens, C., and Antonov, J. I.: World Ocean Atlas 2001, NOAA Atlas NESDIS 52, NOAA, Silver Spring, Md, p. 392pp., 2002.

Curry, B., Lee, C., Petrie, B., Moritz, R., and Kwok, R.: Multiyear volume, liquid freshwater, and sea ice transports through Davis Strait, 2004–10, J. Phys. Oceanogr., 44, 1244–1266, doi:10.1175/JPO-D-13-0177.1, 2014.

30 Dickson, A. G., Sabine, C. L., and Christian, J. R.: Guide to best practices for ocean CO_2 measurements, Tech. rep., PICES Special Publication 3, 191 pp., 2007.

Dutay, J.-C., Bullister, J. L., Doney, S. C., Orr, J. C., Najjar, R., Caldeira, K., Campin, J.-M., Drange, H., Follows, M., Gao, Y., et al.: Evaluation of ocean model ventilation with CFC-11: comparison of 13 global ocean models, Ocean Model., 4, 89–120, doi:10.1016/S1463-5003(01)00013-0, 2002.

35 Gattuso, J.-P. and Hansson, L.: Ocean acidification, Oxford University Press, Oxford, 2011.

Gent, P. R. and Mcwilliams, J. C.: Isopycnal mixing in ocean circulation models, J. Phys. Oceanogr., 20, 150–155, doi:10.1175/1520-0485(1990)020<0150:IMIOCM>2.0.CO;2, 1990.

Gruber, N., Sarmiento, J. L., and Stocker, T. F.: An improved method for detecting anthropogenic CO2 in the oceans, Global Biogeochem. Cycles, 10, 809–837, doi:10.1029/96GB01608, 1996.

Hall, T. M., Haine, T. W., and Waugh, D. W.: Inferring the concentration of anthropogenic carbon in the ocean from tracers, Global Biogeochem. Cycles, 16, doi:10.1029/2001GB001835, 2002.

5   Jakobsson, M.: Hypsometry and volume of the Arctic Ocean and its constituent seas, Geochem. Geophys., 3, 1–18, doi:10.1029/2001GC000302, 2002.

Jakobsson, M., Cherkis, N., Woodward, J., Macnab, R., and Coakley, B.: New grid of Arctic bathymetry aids scientists and mapmakers, Eos, Trans. Amer. Geophys. Union, 81, 89–96, doi:10.1029/00EO00059, 2000.

Jeansson, E., Olsen, A., Eldevik, T., Skjelvan, I., Omar, A. M., Lauvset, S. K., Nilsen, J. E. O., Bellerby, R. G. J., Johannessen, T., and Falck,
10   E.: The Nordic Seas carbon budget: Sources, sinks, and uncertainties, Global Biogeochem. Cycles, 25, doi:10.1029/2010GB003961, 2011.

Jones, E., Rudels, B., and Anderson, L.: Deep waters of the Arctic Ocean: origins and circulation, Deep Sea Res. Part I Oceanogr. Res. Pap., 42, 737–760, doi:10.1016/0967-0637(95)00013-V, 1995.

Jones, P., Azetsu-Scott, K., Aagaard, K., Carmack, E., and Swift, J.: L.S. St. Laurent 18SN19940724, AOS94 cruise data from the 1994 cruises, CARINA Data Set, doi:10.3334/CDIAC/otg.CARINA_18SN19940724, 2007.

15   Key, R. M., Kozyr, A., Sabine, C. L., Lee, K., Wanninkhof, R., Bullister, J. L., Feely, R. A., Millero, F. J., Mordy, C., and Peng, T.-H.: A global ocean carbon climatology: Results from Global Data Analysis Project (GLODAP), Global Biogeochem. Cycles, 18, doi:10.1029/2004GB002247, 2004.

Khatiwala, S., Primeau, F., and Hall, T.: Reconstruction of the history of anthropogenic CO2 concentrations in the ocean, Nature, 462, 346, doi:10.1038/nature08526, 2009.

20   Khatiwala, S., Tanhua, T., Fletcher, S. M., Gerber, M., Doney, S., Graven, H., Gruber, N., McKinley, G., Murata, A., Ríos, A., et al.: Global ocean storage of anthropogenic carbon, Biogeosciences, 10, 2169–2191, doi:10.5194/bg-10-2169-2013, 2013.

Lauvset, S. K., Key, R. M., and Perez, F. F.: A new global interior ocean mapped climatology: the $1° \times 1°$ GLODAP version 2, Earth Syst. Sci. Data, 8, 325, doi:10.5194/essd-8-325-2016, 2016.

Le Quéré, C., Moriarty, R., Andrew, R., Peters, G., Ciais, P., Friedlingstein, P., Jones, S., Sitch, S., Tans, P., Arneth, A., et al.: Global carbon
25   budget 2014, Earth Syst. Sci. Data, 7, 47–85, doi:10.5194/essd-7-47-2015, 2015.

Ludwig, W., Amiotte-Suchet, P., Munhoven, G., and Probst, J.-L.: Atmospheric CO_2 consumption by continental erosion: present-day controls and implications for the last glacial maximum, Glob. Planet. Change, 16, 107–120, doi:10.1016/S0921-8181(98)00016-2, 1998.

Luo, Y., Boudreau, B. P., and Mucci, A.: Disparate acidification and calcium carbonate desaturation of deep and shallow waters of the Arctic Ocean, Nat. Commun., 7, 12 821, doi:10.1038/ncomms12821, 2016.

30   Lythe, M. B. and Vaughan, D. G.: BEDMAP: A new ice thickness and subglacial topographic model of Antarctica, J. Geophys. Res. Solid Earth, 106, 11 335–11 351, doi:10.1029/2000JB900449, 2001.

Madec, G.: NEMO ocean engine, Note du Pôle de modélisation, Institut Pierre-Simon Laplace (IPSL), France, No 27, ISSN No 1288-1619, 2008.

Madec, G., Delecluse, P., Imbard, M., and Levy, C.: Ocean general circulation model reference manual, Note du Pôle de modélisation, Institut
35   Pierre-Simon Laplace (IPSL), France, 1998.

McClelland, J. W., Déry, S. J., Peterson, B. J., Holmes, R. M., and Wood, E. F.: A pan-arctic evaluation of changes in river discharge during the latter half of the 20th century, Geophys. Res. Lett., 33, doi:10.1029/2006GL025753, 2006.

Meinshausen, M., Vogel, E., Nauels, A., Lorbacher, K., Meinshausen, N., Etheridge, D. M., Fraser, P. J., Montzka, S. A., Rayner, P. J., Trudinger, C. M., Krummel, P. B., Beyerle, U., Canadell, J. G., Daniel, J. S., Enting, I. G., Law, R. M., Lunder, C. R., O'Doherty, S., Prinn, R. G., Reimann, S., Rubino, M., Velders, G. J. M., Vollmer, M. K., Wang, R. H. J., and Weiss, R.: Historical greenhouse gas concentrations for climate modelling (CMIP6), Geosci. Model Dev., 10, 2057–2116, doi:10.5194/gmd-10-2057-2017, 2017.

5 Meybeck, M.: Carbon, nitrogen, and phosphorus transport by world rivers, Am. J. Sci, 282, 401–450, doi:10.2475/ajs.282.4.401, 1982.

Moore, J. K., Doney, S. C., and Lindsay, K.: Upper ocean ecosystem dynamics and iron cycling in a global three-dimensional model, Global Biogeoch. Cycles, 18, doi:10.1029/2004GB002220, 2004.

Olsen, A., Anderson, L. G., and Heinze, C.: Arctic Carbon Cycle: Patterns, Impacts and Possible Changes, in: The New Arctic, edited by Evengård, B., Nymand Larsen, J., and Paasche, Ø., pp. 95–115, Springer International Publishing, Cham, doi:10.1007/978-3-319-17602-
10 4_8, 2015.

Orr, J. C., Monfray, P., Maier-Reimer, E., Mikolajewicz, U., Palmer, J., Taylor, N. K., Toggweiler, J. R., Sarmiento, J. L., Quéré, C. L., Gruber, N., Sabine, C. L., Key, R. M., and Boutin, J.: Estimates of anthropogenic carbon uptake from four three-dimensionsal global ocean models, Global Biogeochem. Cycles, 15, 43–60, doi:10.1029/2000GB001273, 2001.

Orr, J. C., Najjar, R. G., Aumont, O., Bopp, L., Bullister, J. L., Danabasoglu, G., Doney, S. C., Dunne, J. P., Dutay, J.-C., Graven, H., et al.:
15 Biogeochemical protocols and diagnostics for the CMIP6 Ocean Model Intercomparison Project (OMIP), Geosci. Model Dev., 10, 2169, doi:10.5194/gmd-10-2169-2017, 2017.

Popova, E., Yool, A., Aksenov, Y., and Coward, A.: Role of advection in Arctic Ocean lower trophic dynamics: A modeling perspective, J. Geophys. Res.: Oceans, 118, 1571–1586, doi:10.1002/jgrc.20126, 2013.

Proshutinsky, A., Steele, M., and Timmermans, M.-L.: Forum for Arctic Modeling and Observational Synthesis (FAMOS): Past, current, and
20 future activities, J. Geophys. Res.: Oceans, 121, 3803–3819, doi:10.1002/2016JC011898, 2016.

Rudels, B., Jones, E. P., Anderson, L. G., and Kattner, G.: On the Intermediate Depth Waters of the Arctic Ocean, in: The Polar Oceans and Their Role in Shaping the Global Environment, edited by Johannessen, O. M., Muench, R. D., and Overland, J. E., pp. 33–46, American Geophysical Union, Washington DC, doi:10.1029/GM085p0033, 1994.

Rudels, B., Marnela, M., and Eriksson, P.: Constraints on estimating mass, heat and freshwater transports in the Arctic Ocean: An exercise,
25 in: Arctic–Subarctic Ocean Fluxes, pp. 315–341, Springer, Dordrecht, Netherlands, 2008.

Sabine, C. L., Feely, R. A., Gruber, N., Key, R. M., Lee, K., Bullister, J. L., Wanninkhof, R., Wong, C., Wallace, D. W., Tilbrook, B., et al.: The oceanic sink for anthropogenic CO2, Science, 305, 367–371, doi:10.1126/science.1097403, 2004.

Sarmiento, J. L., Orr, J. C., and Siegenthaler, U.: A perturbation simulation of CO2 uptake in an ocean general circulation model, J. Geophys. Res.: Oceans, 97, 3621–3645, doi:10.1029/91JC02849, 1992.

30 Schauer, U., Beszczynska-Möller, A., Walczowski, W., Fahrbach, E., Piechura, J., and Hansen, E.: Variation of measured heat flow through the Fram Strait between 1997 and 2006, in: Arctic–Subarctic Ocean Fluxes, pp. 65–85, Springer, Dordrecht, Netherlands, 2008.

Semiletov, I., Pipko, I., Gustafsson, Ö., Anderson, L. G., Sergienko, V., Pugach, S., Dudarev, O., Charkin, A., Gukov, A., Bröder, L., et al.: Acidification of East Siberian Arctic Shelf waters through addition of freshwater and terrestrial carbon, Nat. Geosci., 9, 361–365, doi:10.1038/ngeo2695, 2016.

35 Skagseth, Ø., Furevik, T., Ingvaldsen, R., Loeng, H., Mork, K. A., Orvik, K. A., and Ozhigin, V.: Volume and heat transports to the Arctic Ocean via the Norwegian and Barents Seas, in: Arctic–Subarctic Ocean Fluxes, pp. 45–64, Springer, Dordrecht, Netherlands, 2008.

Smedsrud, L. H., Ingvaldsen, R., Nilsen, J. E. Ø., and Skagseth, Ø.: Heat in the Barents Sea: transport, storage, and surface fluxes, Ocean Sci., 6, 219–234, doi:10.5194/os-6-219-2010, 2010.

Smith, W. H. and Sandwell, D. T.: Global sea floor topography from satellite altimetry and ship depth soundings, Science, 277, 1956–1962, doi:10.1126/science.277.5334.1956, 1997.

Steinacher, M., Joos, F., Frolicher, T. L., Plattner, G.-K., and Doney, S. C.: Imminent ocean acidification in the Arctic projected with the NCAR global coupled carbon cycle-climate model, Biogeosciences, 6, 515–533, doi:10.5194/bg-6-515-2009, 2009.

5 Straneo, F. and Saucier, F.: The outflow from Hudson Strait and its contribution to the Labrador Current, Deep Sea Res. Part I Oceanogr. Res. Pap., 55, 926–946, doi:10.1016/j.dsr.2008.03.012, 2008.

Stöven, T., Tanhua, T., Hoppema, M., and Wilken-Jon, v. A.: Transient tracer distributions in the Fram Strait in 2012 and inferred anthropogenic carbon content and transport, Ocean Sci., 12, 319–333, doi:10.5194/os-12-319-2016, 2016.

Takahashi, T., Broecker, W. S., and Langer, S.: Redfield ratio based on chemical data from isopycnal surfaces, J. Geophys. Res.: Oceans, 90,
10 6907–6924, doi:10.1029/JC090iC04p06907, 1985.

Tanhua, T., Jones, E. P., Jeansson, E., Jutterström, S., Smethie, W. M., Wallace, D. W., and Anderson, L. G.: Ventilation of the Arctic Ocean: Mean ages and inventories of anthropogenic CO_2 and CFC-11, J. Geophys. Res.: Oceans, 114, doi:10.1029/2008JC004868, 2009.

Taylor, K. E., Stouffer, R. J., and Meehl, G. A.: An Overview of CMIP5 and the Experiment Design, Bull. Am. Meteorol. Soc., 93, 485–498, doi:10.1175/bams-d-11-00094.1, https://doi.org/10.1175/bams-d-11-00094.1, 2012.

15 Tegen, I. and Fung, I.: Contribution to the atmospheric mineral aerosol load from land surface modification, J. Geophys. Res.: Atmos., 100, 18 707–18 726, doi:10.1029/95JD02051, 1995.

Vancoppenolle, M., Fichefet, T., Goosse, H., Bouillon, S., Madec, G., and Maqueda, M. A. M.: Simulating the mass balance and salinity of Arctic and Antarctic sea ice. 1. Model description and validation, Ocean Model., 27, 33 – 53, doi:10.1016/j.ocemod.2008.10.005, 2009.

Walsh, J. E., Chapman, W. L., and Fetterer, F.: Gridded Monthly Sea Ice Extent and Concentration, 1850 Onward, Version 1. [1979 to 2010],
20 doi:http://dx.doi.org/10.7265/N5833PZ5, Boulder, Colorado USA. NSIDC: National Snow and Ice Data Center, 2015.

Waugh, D. W., Haine, T. W., and Hall, T. M.: Transport times and anthropogenic carbon in the subpolar North Atlantic Ocean, Deep Sea Res. Part I Oceanogr. Res. Pap., 51, 1475–1491, doi:10.1016/j.dsr.2004.06.011, 2004.

Willey, D. A., Fine, R. A., Sonnerup, R. E., Bullister, J. L., Smethie Jr., W. M., and Warner, M. J.: Global oceanic chlorofluorocarbon inventory, Geophys. Res. Lett., 31, L01303, doi:10.1029/2003GL018816, 2004.

25 Woodgate, R.: Arctic Ocean circulation: Going around at the top of the world, Nat. Edu. Knowl., 4, 8, 2013.

Woodgate, R. A., Weingartner, T., and Lindsay, R.: The 2007 Bering Strait oceanic heat flux and anomalous Arctic sea-ice retreat, Geophys. Res. Lett., 37, doi:10.1029/2009GL041621, l01602, 2010.

Yang, D.: An improved precipitation climatology for the Arctic Ocean, Geophys. Res. Lett., 26, 1625–1628, doi:10.1029/1999GL900311, 1999.

Table 1. Selected physical coefficients and parameters for ORCA2, ORCA05, and ORCA025.

Configuration	Lateral diffusivity	Lateral viscosity	Eddy parameterization
ORCA2	2000 $m^2\ s^{-1}$	4 $\times10^4$ m^2 s^{-1} [a]	2000 m^2 s^{-1}
ORCA05	600 $m^2\ s^{-1}$	-4 $\times10^{11}$ m^2 s^{-1}	1000 m^2 s^{-1}
ORCA025	300 $m^2\ s^{-1}$	-1.5 $\times10^{11}$ m^2 s^{-1}	none

[a] reduced to 2100 m^2 s^{-1} in the tropics (except along Western boundaries)

[b] Lateral diffusivity and viscosity coefficients decrease towards the poles proportional to the grid size.

Table 2. Fitted parameters for the perturbation approach for the traces starting in 1765 (P1765) and in 1870 (P1870).

Parameter	P1765	P1870
a_0	1.7481	1.8302
a_1	-3.2813×10^{-2}	-3.4631×10^{-2}
a_2	4.1855×10^{-4}	4.3614×10^{-4}
b_0	3.9615×10^{-3}	4.0105×10^{-3}
b_1	-7.3733×10^{-5}	-7.3386×10^{-5}
b_2	5.4759×10^{-5}	5.1199×10^{-5}

Table 3. Grid size in the Arctic Ocean and volumes by basin as a function of model resolution.

Configuration	Horizontal grid (km)			Volume (10^6 km^3)					
					Basins				
	Mean	Min	Max	Arctic	Nansen	Amundsen	Makarov	Canada
ORCA2	120.8	63.3	180.5	14.3	2.8	3.2	2.2	4.7
ORCA05	29.0	9.4	41.3	13.3	2.6	2.7	1.9	4.9
ORCA025	14.4	3.2	20.5	13.3	2.3	2.9	1.8	5.0

Table 4. Lateral transport of water and C_{ant} across Arctic Ocean boundaries. Simulated values are calculated for the same time period.

Lateral water transport (Sv)

	Model configuration			Observations	Year	Sources
	ORCA2	ORCA05	ORCA025			
Fram Strait	-1.76	-1.75	-1.80	-2.0 ± 2.7	1997–2006	Schauer et al. (2008)
	-1.76	-1.42	-1.46	-1.7	1980–2005	Rudels et al. (2008)
Barents Sea	1.20	2.50	2.77	2.0	2003–2005	Skagseth et al. (2008)
	1.04	2.42	2.78	2.0	1997–2007	Smedsrud et al. (2010)
Bering Strait	1.02	1.29	1.49	0.8 ± 0.2	1991–2007	Woodgate et al. (2010)
CAA	-0.29	-2.00	-2.59	-2.7 ± 0.2	2004–2013	Curry et al. (2014)
Total transport	-0.12	-0.16	-0.18			

Lateral C_{ant} fluxes (Tg C yr^{-1})

	Model configuration					Observations	Year	Sources
	ORCA2	ORCA05	ORCA025	P1765	P1870			
Fram Strait	-14	-10	-6	-12	-10	-1 ± 17	2002	Jeansson et al. (2011)
	-14	-5	7	-6	-4	-12	2012	Stöven et al. (2016)
Barents Sea	14	38	44	41	36	41 ± 8	2002	Jeansson et al. (2011)
Bering Strait	16	20	24	22	20	18	$2000 - 2010^{a}$	Olsen et al. (2015)
CAA	-4	-25	-31	-26	-23	-29	$2000 - 2010^{a}$	Olsen et al. (2015)
Summed lateral flux	17	28	37	30	29	29	$2000 - 2010^{a}$	Olsen et al. (2015)

[a] Year or period impossible to identify exactly as C_{ant} and velocity measurements are not from the same year

Table 5. Total inventory, its change during 1960–2012, cumulative air-sea flux, and lateral flux of C_{ant} in Pg C

	Model configuration				
	ORCA2	ORCA05	ORCA025	P1765	P1870
C_{ant} **inventory**[a]					
C_{ant} in 2002[b]	1.47 (1.88)	1.81 (2.25)	2.06 (2.47)	2.04	1.63
C_{ant} in 2005[c]	1.56 (1.97)	1.96 (2.37)	2.21 (2.62)	2.15	1.74
Inventory change (1960-2012)					
Total Arctic	1.04	1.50	1.91	1.39	1.34
Nansen Basin	0.14	0.33	0.29	0.30	0.30
Amundsen Basin	0.13	0.27	0.33	0.25	0.24
Makarov Basin	0.14	0.20	0.32	0.19	0.18
Canada Basin	0.29	0.34	0.57	0.31	0.29
Cumulative fluxes (1960-2012)					
Air-Sea flux	0.29	0.42	0.47	0.23	0.22
Lateral flux of C_{ant} [d]	0.75	1.08	1.45	1.17	1.12
Fram Strait	-0.59	-0.29	0.04	-0.36	-0.25
Barents Sea	0.68	1.51	1.70	1.68	1.44
Bering Strait	0.64	0.77	0.89	0.89	0.77
CAA	-0.18	-0.99	-1.25	-1.13	-0.92
Summed lateral flux	0.55	1.00	1.39	1.09	1.04

[a] Numbers in brackets show the corrected value by the perturbation approach

[b] Data-based inventory in 2002: 2.95 Pg C (GLODAPv2)

[c] Data-based inventory in 2005: 3.03 Pg C (2.5-3.3) (Tanhua et al., 2009)

[d] Computed as inventory change minus cumulative air-sea flux

Biogeosciences
Discussions

Open Access

EGU
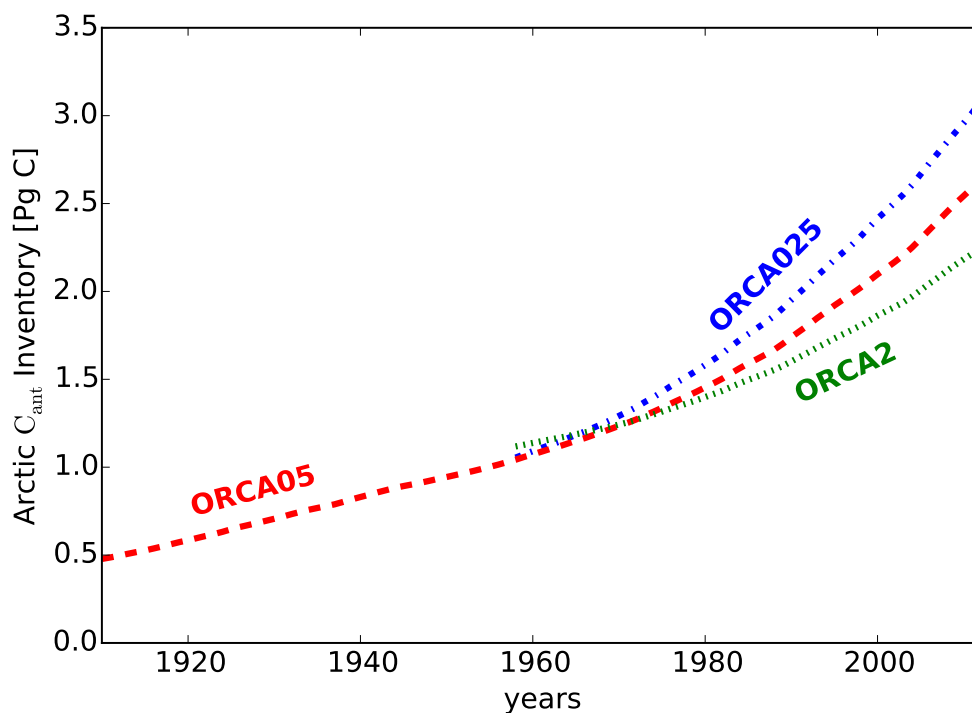
Figure 1. Arctic Ocean C_{ant} inventory for the three biogeochemical simulation resolutions corrected for the late starting date. The intermediate-resolution model (ORCA05 - red dashed) was integrated from 1870 to 2012. The high-resolution model (ORCA025 - blue dash-dot) and the low-resolution model (ORCA2 - dotted green) were initialized with the ORCA05 output at the end of 1957 and integrated from 1958 to 2012. The discontinuity for ORCA2 in 1958 is due to its larger total volume of water when integrated across the Arctic domain (Table 3).
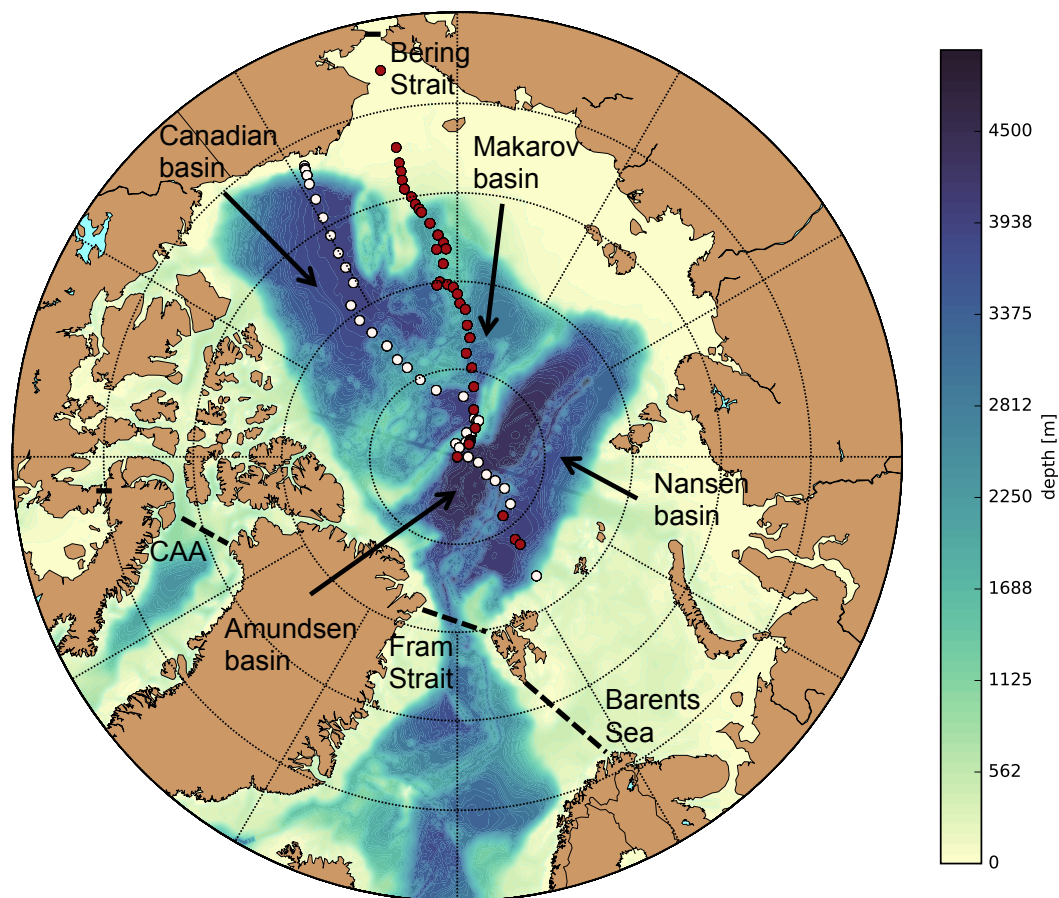
Figure 2. CFC-12 stations occupied during the AOS94 (red) and Beringia 2005 expedition (white). The filled-color scheme indicates the bathymetry of the Arctic Ocean, while the four dashed lines show the boundaries used in this study.
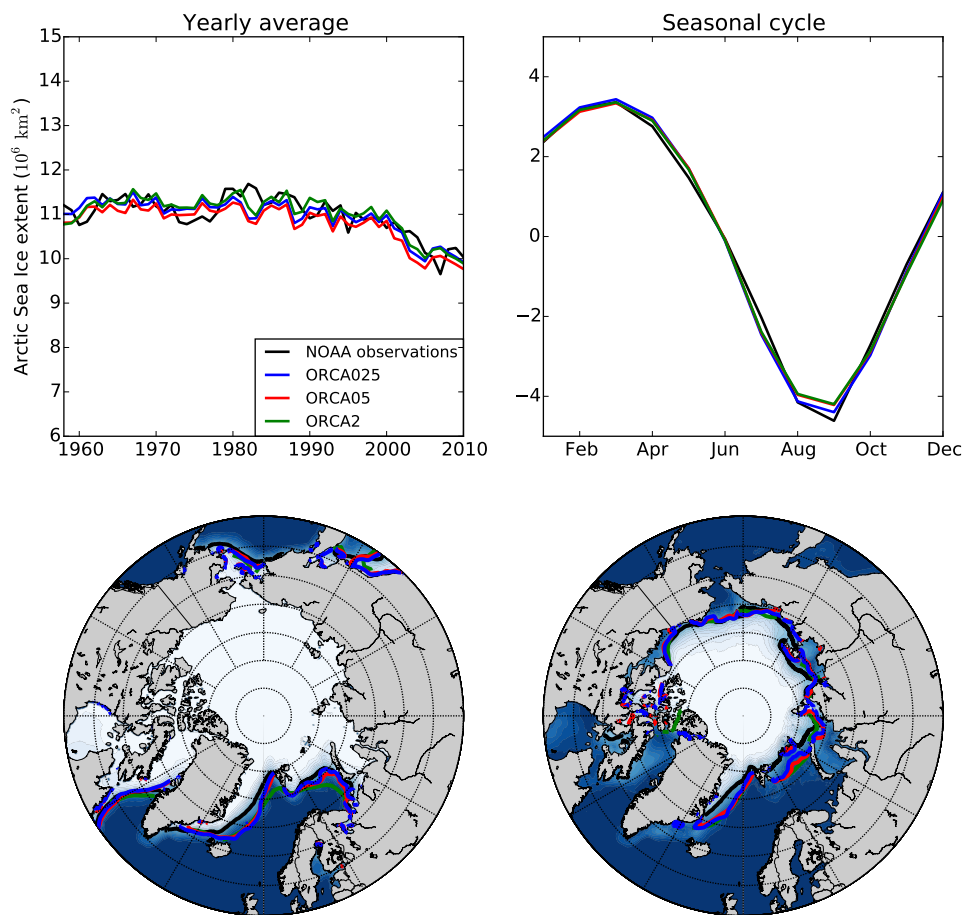
Figure 3. Sea-ice concentration in the Arctic from 1960 to 2012 comparing microwave-based observations from NOAA (black) to simulated results from ORCA2 (green), ORCA05 (red), and ORCA025 (blue). Shown are the yearly average (top left), and after detrending, the average (climatological) seasonal cycle over 1958–2010 (top right), average sea-ice extent in winter (December, January, February) (bottom left), and summer (bottom right). The lines on the maps show the 50% sea-ice cover for the three model resolutions and the observations. The white color indicates the observed sea-ice concentration.
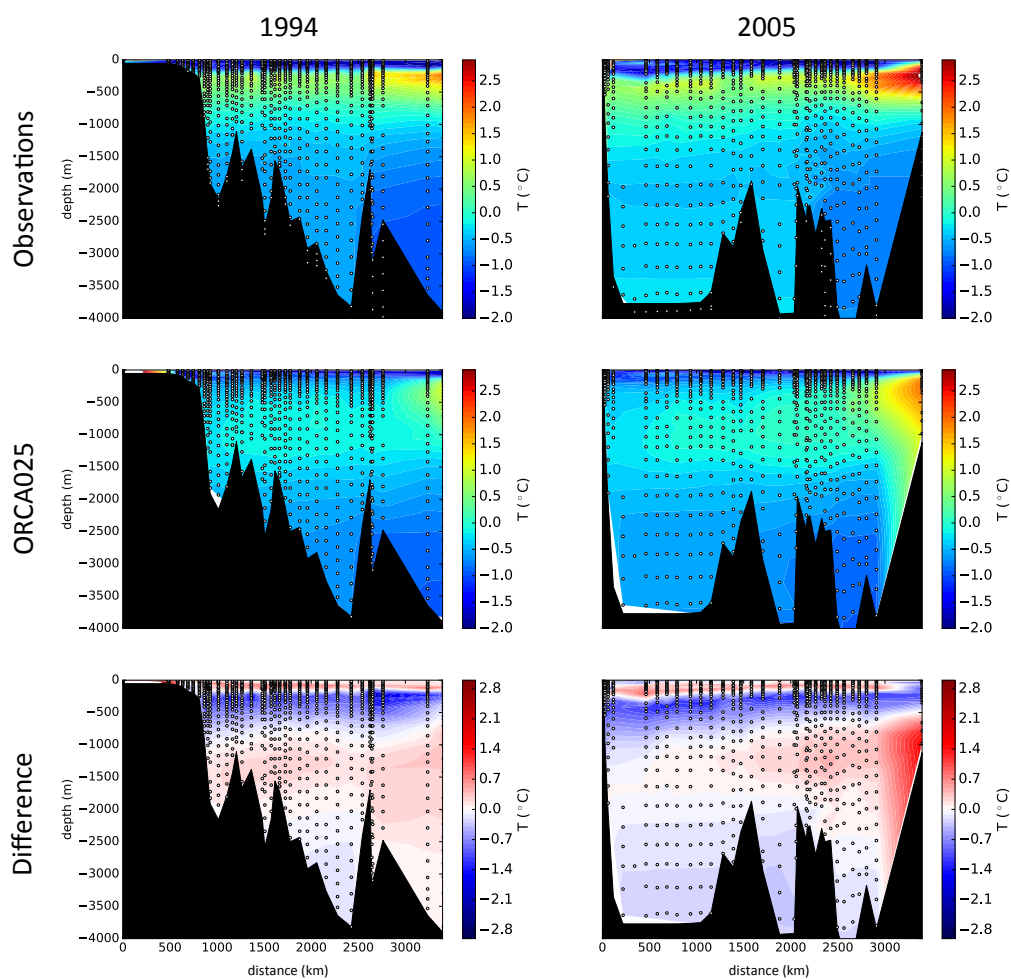
Figure 4. Temperature along the 1994 Arctic Ocean Section (AOS94) cruise (left) and the Beringia/HOTRAX 2005 expedition (right), both trans-Arctic transects (Fig. 2). The observations (top) are compared to simulated results from ORCA025 averaged over summer of the respective year (middle). The difference (model − observations) is shown at the bottom. The location of the sections is shown in Fig. 2.
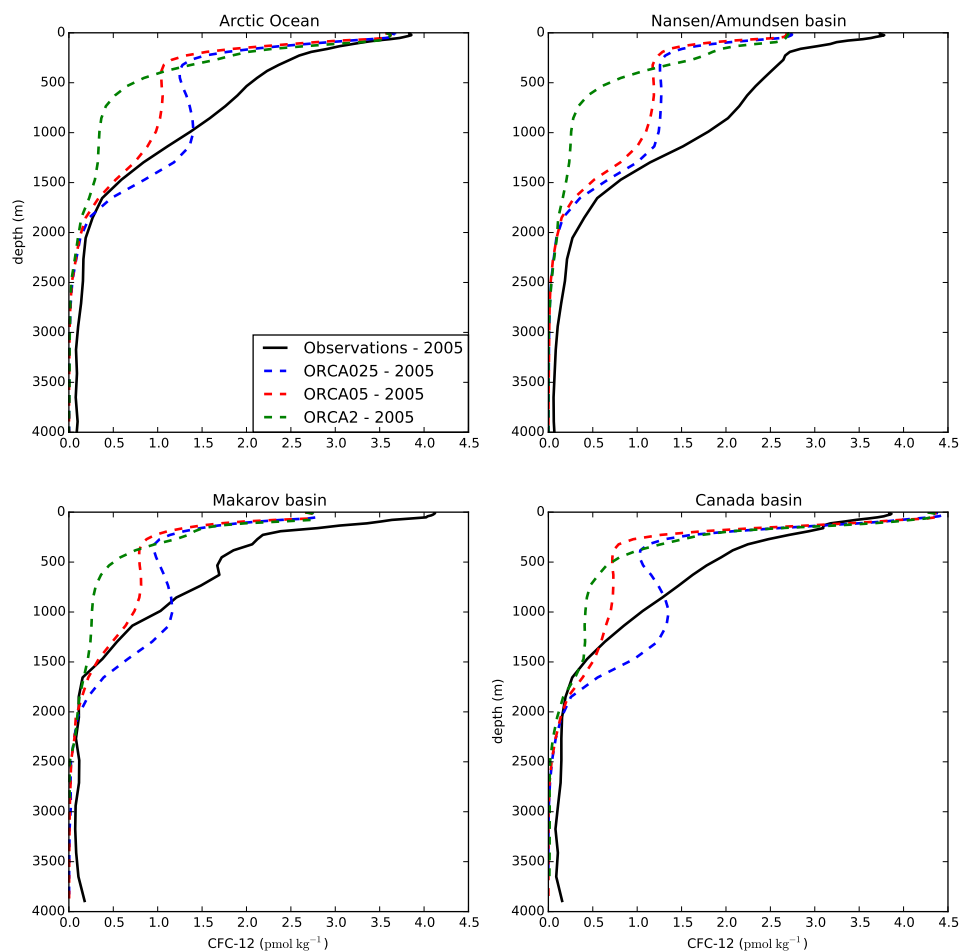
Figure 5. Profiles of CFC-12 for observations (black) and the ORCA025 (blue), ORCA05 (red), and ORCA2 (green) model along the 2005 sections. Shown are distance-weighted mean across each section (top left), the Nansen and Amundsen basins (top right), the Canada basin (bottom left), and the Makarov basin (bottom right).
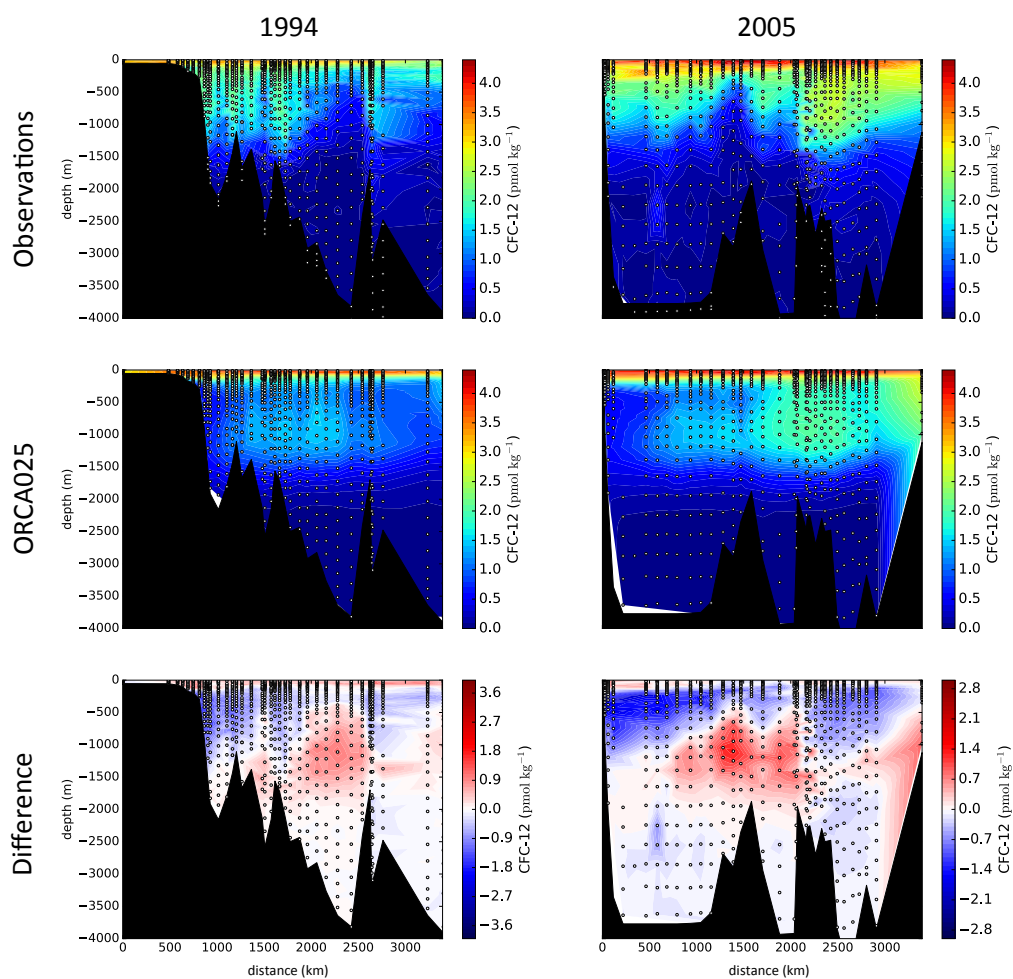
Figure 6. CFC-12 sections along the AOS94 section (left) and the Beringia section (right). The observations (top) are compared to the simulated summer means (middle) and model−data difference is shown at the bottom.
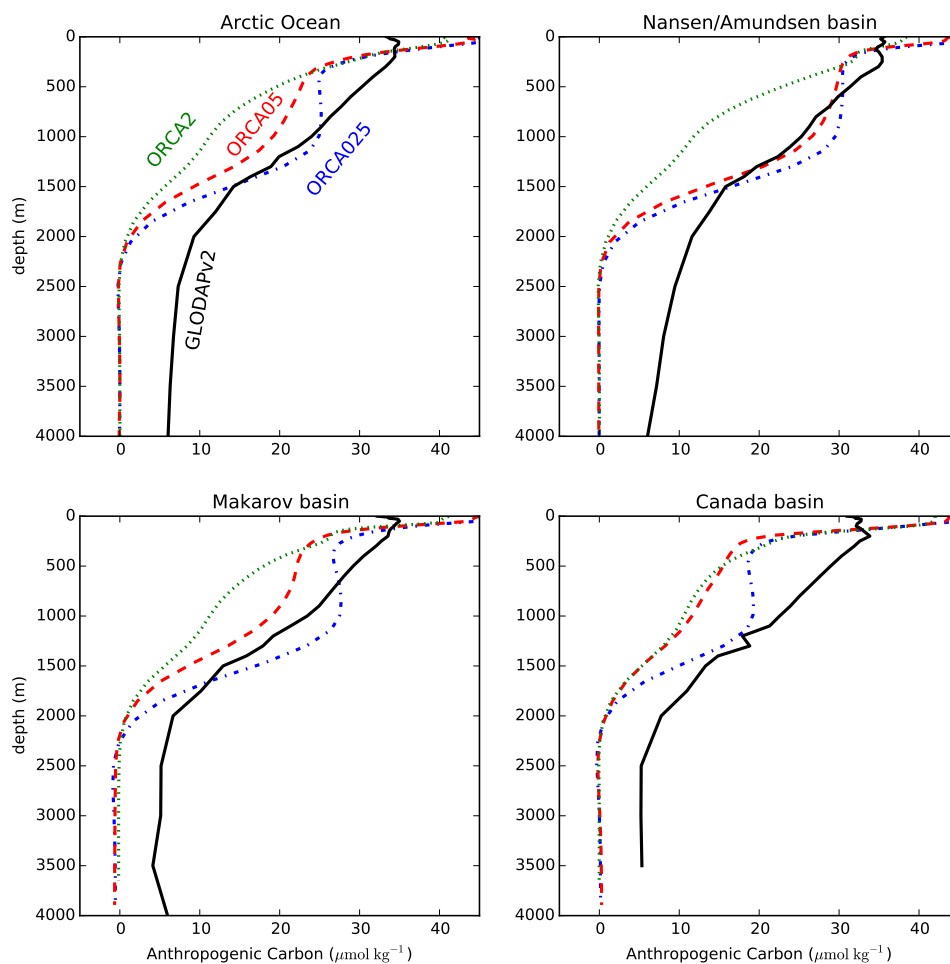
Figure 7. Area-weighted vertical profiles of C_{ant} concentrations for GLODAPv2 data-based estimates (black), ORCA2 (green), ORCA05 (red) and ORCA025 (blue) over the entire Arctic Ocean corrected for the starting year by the perturbation approach simulations.
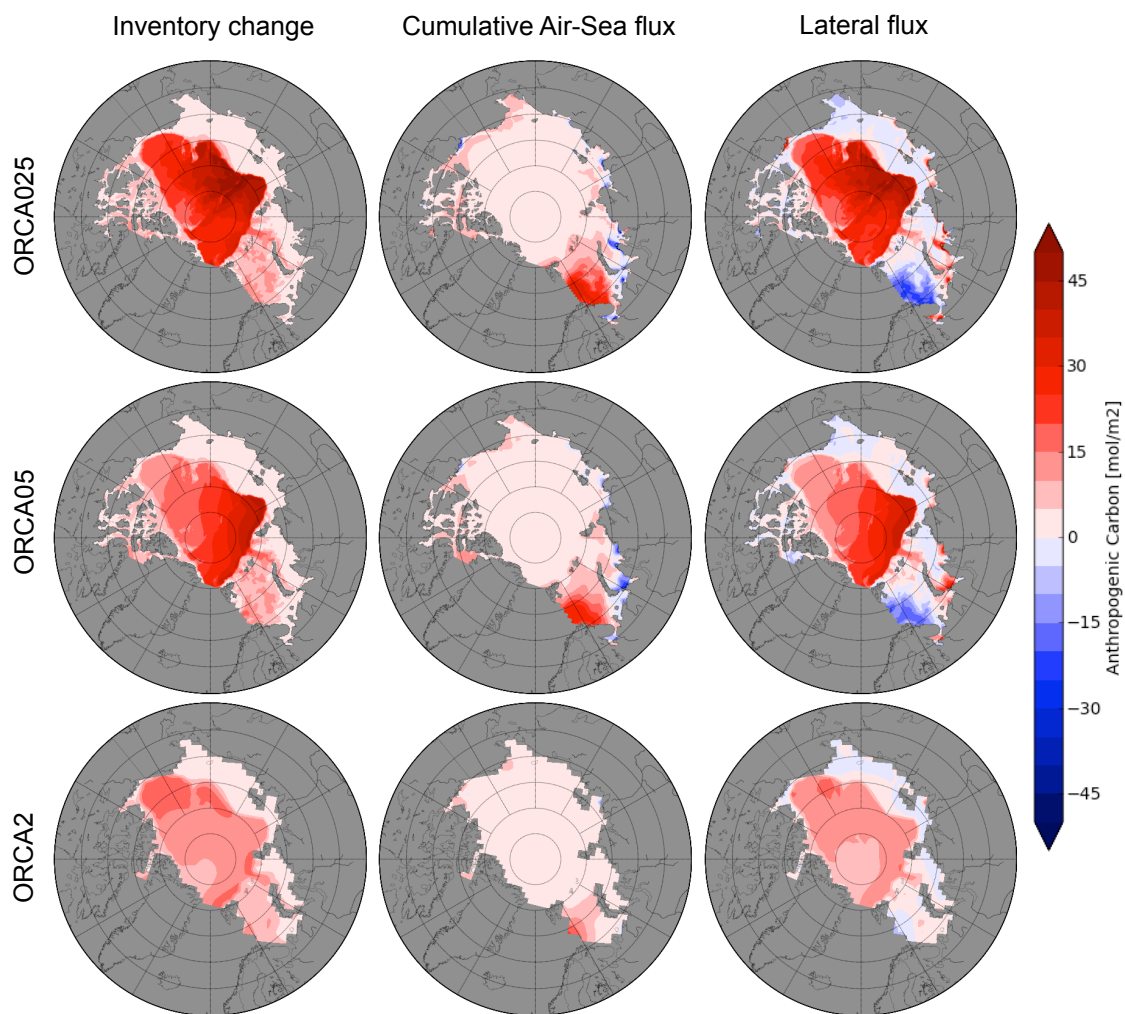
Figure 8. Inventory change (left), cumulative air-sea flux (middle), and the lateral flux calculated as the difference of inventory change and air-sea flux (right) of C_{ant} for the period from 1960 to 2012 for the ORCA025 (top), ORCA05 (center), and ORCA2 (bottom) model configurations.
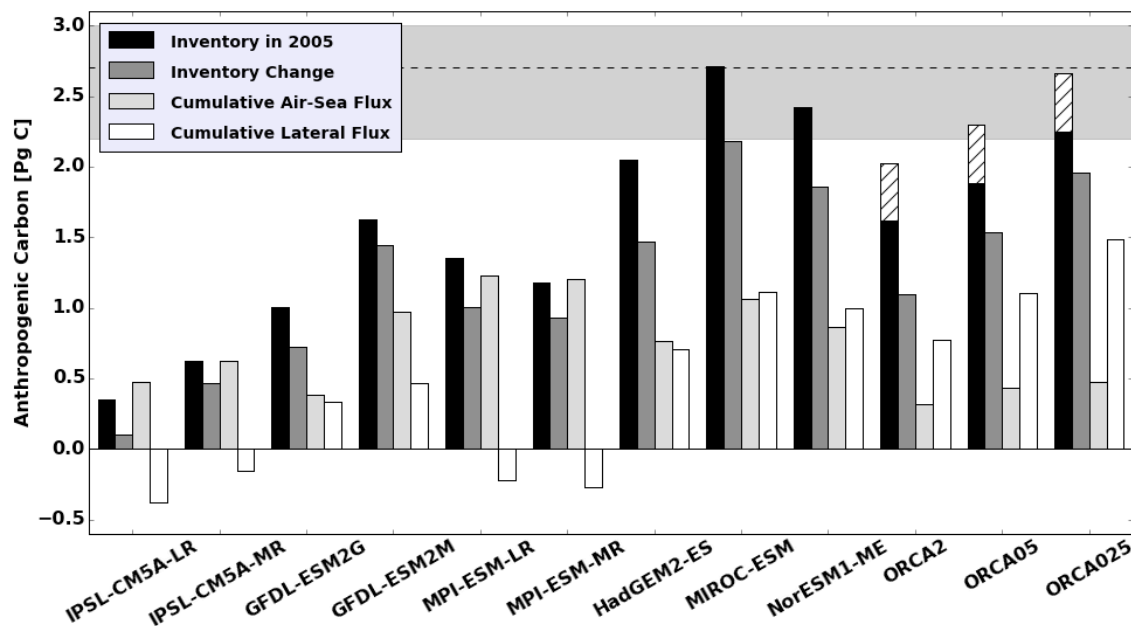
Figure 9. Comparison of results for the Arctic Ocean from the three resolutions of NEMO-PISCES and the nine Earth System Models that participated in CMIP5. Shown are the C_{ant} inventory in 2005 (black), the inventory change of C_{ant} (dark grey) between 1960 and 2012, the corresponding cumulative air-sea flux of C_{ant} (light grey) and the cumulative lateral flux of C_{ant} (white). Also indicated are the corrected estimate by Tanhua et al. (2009) (dashed black line) and the associated uncertainty estimates (grey background). The inventory correction of the biogeochemical simulations using the perturbation approach is added to the results of the biogeochemical simulations as striped bars.
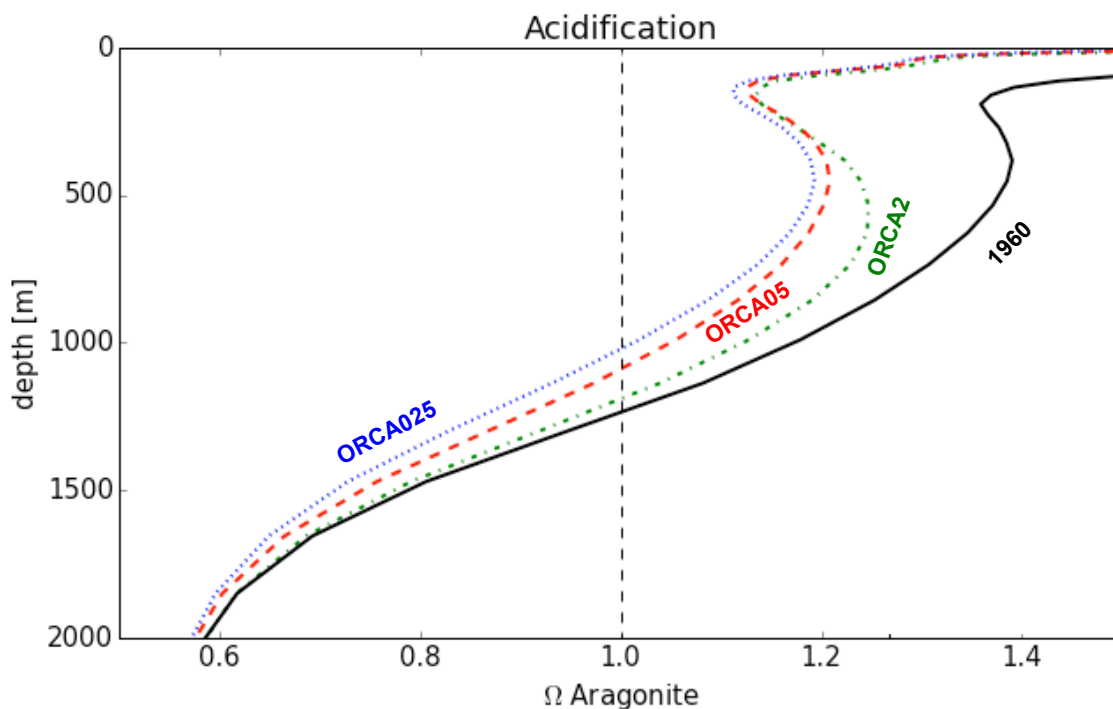
Figure 10. Profiles of Ω_A after the early industrial period period simulated only in ORCA05 (1870–1957), after intializing the other models in 1958. Results are shown for ORCA05 in 1960 (black solid) as well as ORCA2 (green dot-dash), ORCA05 (red dashes), and ORCA025 (blue dots) in 2012. The vertical black dashed line indicates the chemical threshold where $\Omega_A = 1$. Where that vertical line intersects the other curves indicates the depth of the ASH in each case.
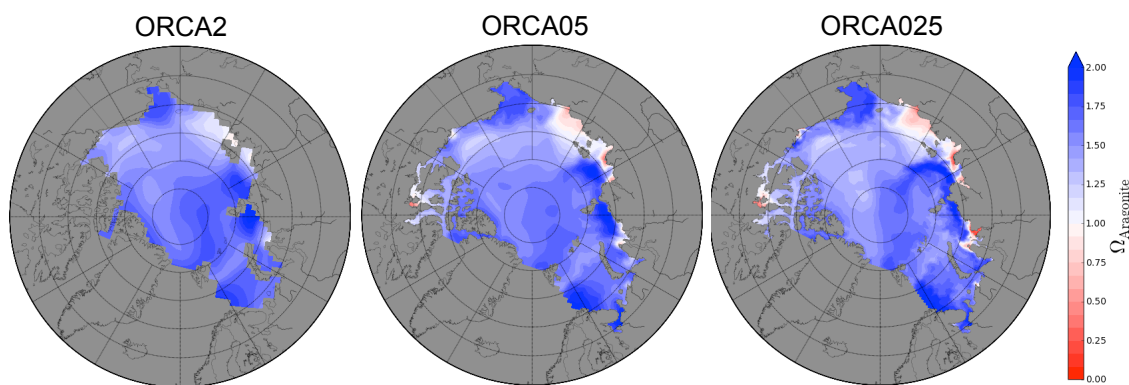

Figure 11. Surface Ω_A for ORCA2, ORCA05 and ORCA025 (from left to right) in August 2012.